RSC Advances

ROYAL SOCIETY OF CHEMISTRY

PAPER

View Article Online
View Journal | View Issue

Check for updates

Cite this: *RSC Adv.*, 2025, **15**, 48025

Transforming seafood waste into therapeutic potential: cholecalciferol-loaded marine bone as a biocompatible antimicrobial and biomedical therapeutic agent

Samar M. Mahgoub,[a] Ahmed A. Allam,[b] Abdullah S. Alawam,[b] Hassan A. Rudayni,[b] Doaa R. I. Abdel-Gawad,[c] Asmaa Elrafey,[d] Rania Abdelazeem,[d] Zienab E. Eldin[a] and Rehab Mahmoud *[e]

Received 3rd July 2025
Accepted 5th November 2025

DOI: 10.1039/d5ra04737d

rsc.li/rsc-advances

The seafood processing industry generates significant shell waste, such as cuttlefish bone (CFB), which poses environmental challenges but is rich in minerals suitable for biomedical applications. In this study, CFB was transformed into calcinated cuttlefish bone (CCFB) with a high specific surface area (92.64 m^2 g^{-1}) and pore volume (0.16 cm^3 g^{-1}), enabling efficient loading of cholecalciferol (vitamin D3; 89.7% loading efficiency). Comprehensive characterization confirmed the structural integrity and adsorption capacity of the material. The incorporation of cholecalciferol into CCFB offered distinct functional advantages over CCFB alone. Cholecalciferol-loaded CCFB exhibited enhanced biocompatibility and great cytotoxic effect against the cancerous cells, as evidenced low cell viability at 500 μg mL^{-1}, superior antimicrobial activity against *Staphylococcus aureus* (4-log reduction in viability at 5 μg mL^{-1}), and increased antioxidant capacity (62 nmol GSH per mg protein). The composite also showed ∼50% lower lactate dehydrogenase (LDH) release compared to CCFB alone, indicating improved detoxifying properties. *In vitro* release studies revealed a controlled and sustained release profile of cholecalciferol from the CCFB matrix (94.14% release over 36 h), supporting its potential for prolonged therapeutic action. These combined properties position cholecalciferol-loaded CCFB as a multifunctional, waste-derived biomaterial with improved efficacy for antimicrobial therapy and controlled drug delivery. This work demonstrates a sustainable strategy for seafood waste valorization, offering both environmental benefits and innovative biomedical solutions.

1 Introduction

The seafood processing industry generates significant amounts of shell waste, which can be expensive to dispose of and can pose environmental and health risks.[1] Shellfish waste, classified as a category III animal by-product, must be carefully managed according to regulations if it's intended for reuse in the food or feed chain. With growing environmental awareness and strict laws, there's a pressing need for safe waste disposal. One common type of discarded material is the internal shell of *Sepia*, also known as cuttlefish bone (CFB). This hard, brittle structure is primarily composed of aragonite and is chambered and gas-filled, aiding buoyancy. The genus *Sepia* comprises numerous species of cuttlefish distributed worldwide, each exhibiting distinct biological and structural characteristics. Variations among *Sepia* species include differences in cuttlebone composition, mineral content, porosity, and mechanical properties, which can affect their suitability for various biomedical applications. For example, *Sepia* officinalis is widely studied for its dense, calcium-rich cuttlebone, whereas other species may differ in organic matrix composition or trace element content that influence biocompatibility and functional performance. Recognizing these species-specific differences is crucial for optimizing the valorization of cuttlefish bone waste and tailoring its use in therapeutic and antimicrobial materials.

Recent systematic reviews have highlighted the increasing interest in cuttlefish-bone-derived biomaterials for regenerative medicine, dentistry, and tissue engineering applications, with

---

[a] *Materials Science and Nanotechnology Department, Faculty of Postgraduate Studies for Advanced Sciences, Beni-Suef University, Egypt. E-mail: miramar15@yahoo.com; zienabessam@zewailcity.edu.eg*

[b] *Department of Biology, College of Science, Imam Mohammad Ibn Saud Islamic University (IMSIU), Riyadh 11623, Saudi Arabia. E-mail: asalawam@imamu.edu.sa; HARUDAYNI@imamu.edu.sa; aallam@imamu.edu.sa*

[c] *Toxicology and Forensic Medicine Department, Faculty of Veterinary Medicine, Beni-Suef University, Beni-Suef, 62511, Egypt. E-mail: dooaramadan1991@vet.bsu.edu.eg*

[d] *Environmental Science and Industrial Development Department, Faculty of Postgraduate Studies for Advanced Sciences, Beni-Suef University, Beni-Suef, Egypt. E-mail: asmaa_elrafey@hotmail.com; raniashaban333@gmail.com*

[e] *Department of Chemistry, Faculty of Science, Beni-suef University, Beni-suef 62528, Egypt. E-mail: rehabkhaled@science.bsu.edu.eg*

studies focusing on hydroxyapatite (HAp) synthesis, scaffold development, dental material enhancement, and antimicrobial properties.[2,3] (CFB) are frequently used as calcium-rich dietary supplements for caged birds,[4] while shell powder serves purposes such as antacid or absorbent. (CFB) is rich in calcium and its powder is used in toothpaste preparation. CFB powder holds promise for biomedical applications and has a rich history of use in oral health biomedicine in both India and China.[5] Traditionally, it has been employed to address diverse ear conditions, control bleeding, and improve renal function.[6] Additionally, the inorganic composition of (CFB) includes small quantities of magnesium, sodium, and strontium alongside calcium carbonate ($CaCO_3$) in the aragonite form. These minerals play crucial roles in bone recovery processes.[7,8] Previous studies have demonstrated that cuttlefish bone can be successfully transformed into hydroxyapatite scaffolds suitable for bone tissue engineering applications, showing good biocompatibility and potential for further development in dynamic culture systems.[9,10] Shell waste presents an opportunity for producing valuable bioactive compounds like chitin and chitosan. Chitin, chemically related to cellulose, is a key component of the exoskeletons of insects, crustaceans, and arachnids.[11] Chitosan, a derivative of chitin, has garnered attention for its antimicrobial properties, biocompatibility, and biodegradability. These compounds have diverse applications in industries including papermaking, textiles, pharmaceuticals, cosmetics, and food.[12–17] Unlike chitosan-based carriers that rely on electrostatic membrane interactions.[18,19] CCFB is derived from calcined aragonite ($CaCO_3$), transforming into a mesoporous CaO/MgO scaffold with distinct physicochemical properties. This mineral structure enables mechanical disruption of bacterial membranes, complementing cholecalciferol's bioactivity. Moreover, crustacean and mollusk shells can enhance water quality by reducing levels of organic pollutants and heavy metals. Utilizing shell waste for wastewater treatment offers both environmental and economic benefits.[20] Recent studies have demonstrated the potential of cuttlefish bone powder as an efficient solid-phase extraction sorbent for pharmaceutical compounds from environmental water samples, further supporting its versatility in environmental applications.[21] In addition to their environmental and biomedical promise, recent economic studies have emphasized the cost-effectiveness of repurposing seafood waste into functional biomaterials. Utilizing shell waste not only reduces disposal costs but also offers a low-cost source of high-value compounds. For instance, transforming cuttlefish bone into calcinated biomaterials has demonstrated substantial savings compared to the synthesis of conventional adsorbents or synthetic drug carriers.[2] Economic modeling from similar valorization efforts shows that using marine waste can reduce raw material costs by over 60%, while simultaneously generating value-added products that support circular bioeconomy goals.[22,23] These findings further support the integration of CFB-derived materials into commercial-scale water treatment, drug delivery, and therapeutic applications, particularly in resource-constrained settings.

There's a growing trend towards symbiotic waste management, where one industry's waste becomes another's resource, benefiting both parties. As a global community, it's crucial to prioritize efforts to improve and safeguard water quality.[24–26] Despite these promising attributes, most previous studies have focused on CFB as a source of calcium or as a simple adsorbent, with limited exploration of its potential as a multifunctional platform for advanced therapeutic delivery or antimicrobial intervention. While recent research has explored biogenic fabrication of hydroxyapatite nanorods from cuttlefish bone with demonstrated bactericidal and biocompatibility properties,[27] the integration of CFB with other bioactive agents for enhanced biomedical performance remains underexplored, and there is a lack of sustainable, waste-derived biomaterials that can simultaneously deliver therapeutic agents and exhibit intrinsic antimicrobial and antioxidant activities. On the other hand, cholecalciferol (vitamin D3) is crucial for maintaining good health, sourced from both skin synthesis and dietary intake. Most people rely on sunlight exposure, specifically UVB radiation, to meet their cholecalciferol needs. UVB rays trigger the conversion of 7-dehydrocholesterol in the skin into cholecalciferol. Factors like season, latitude, time of day, skin color, age, and sunscreen use affect this process. Cholecalciferol deficiency can lead to rickets in children and exacerbate osteoporosis and osteomalacia in adults, causing bone pain. Additionally, it's linked to increased risks of cardiovascular disease, type 1 and type 2 diabetes, and certain cancers, notably colon and prostate cancer. Even in low-latitude regions like Brazil, subclinical cholecalciferol deficiency is common, especially among the elderly.[28] Recent studies have highlighted the immunomodulatory functions of vitamin D, particularly its role in regulating antimicrobial peptide expression and host defense mechanisms, with demonstrated effects against bacterial pathogens including *Staphylococcus aureus*.[29,30] Contemporary research in drug delivery has explored various nanotechnology-based approaches for cholecalciferol delivery, including polymeric nanospheres, nanoemulsions, and nanocellulose-based membranes for controlled release applications.[31–33] One of the leading causes of morbidity and death today is bacterial infections. The development of new bactericidal methods is necessary due to the growing worry about biofilm-associated infections and multidrug-resistant bacterial strains. As a result, new and developing materials based on nanoparticles have received particular interest in the field of antimicrobial therapy.[34] Advanced functional nanomaterials with distinctive chemical and physical properties have been developed as a result of recent developments in nanoscience and nanotechnology. Developing bactericidal drugs to cure fatal microbial infections is made possible by the high surface-area-to-volume ratio of nanoparticles (NPs).[35] However, the synergistic integration of cholecalciferol that is a molecule known for its roles in bone health, immune modulation, and antioxidant defense with marine-derived biomaterials such as CCFB has not been systematically investigated. There is a particular lack of studies evaluating the controlled release, cytocompatibility, and antimicrobial action of cholecalciferol-loaded CCFB composites, especially in the context of sustainable waste valorization.

To address these gaps, this study is the first to transform seafood waste (CFB) into a high-value, calcinated biomaterial

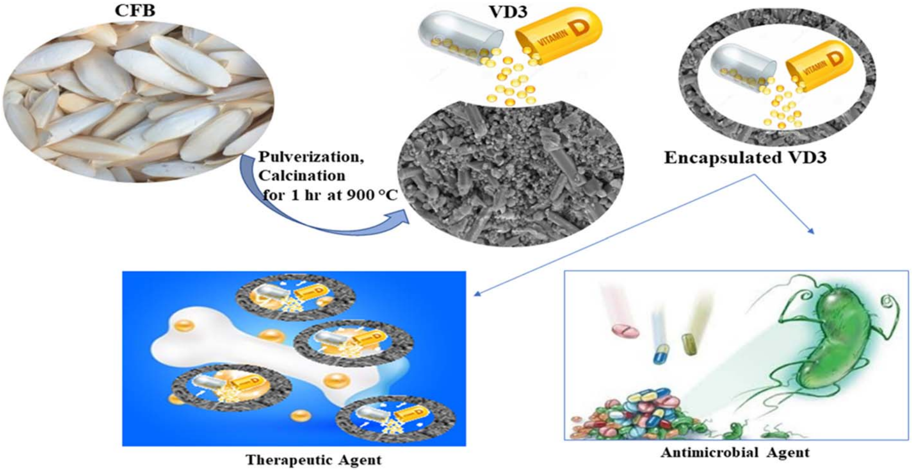

Scheme 1 Overview of the methodology for transforming cuttle fish bone (CFB) into a functional drug delivery system. CFB undergo pulverization, pyrolysis (900 °C, 1 h), and calcination to produce CCFB. The resulting material serves as an encapsulation matrix for cholecalciferol, enabling dual therapeutic and antimicrobial applications.

(CCFB) and load it with cholecalciferol, creating a multifunctional agent that leverages both the mineral and therapeutic properties of its components. Unlike previous studies that have primarily focused on either CFB-derived materials or cholecalciferol delivery systems separately, our approach represents a novel integration of waste valorization with advanced therapeutic delivery. The antimicrobial efficacy, cytotoxic effects, and antioxidant effects of CCFB before and after cholecalciferol loading were systematically evaluated, using robust *in vitro* assays against *Staphylococcus aureus* and MG-63 cell line. This work demonstrates for the first time that cholecalciferol-loaded CCFB exhibits superior antibacterial and antioxidant performance compared to CCFB alone, with a controlled release profile suitable for sustained biomedical applications. By integrating waste valorization with advanced drug delivery and antimicrobial strategies, this study not only proposes a sustainable solution for shell waste management but also introduces a novel biomaterial platform with significant promise for therapeutic and clinical use. The objective of the present study was to evaluate the feasibility of CCFB powder to develop an antimicrobial agent to treat bacterial infection especially *S. aureus*, also estimation of the CCFB, and CCFB-cholecalciferol cytotoxicity, also to study the cholecalciferol-CCFB pharmacokinetics (Scheme 1). Table S1 includes a Comparative analysis of current work against previous literature, highlighting confirmation, contrasts, and extensions in the development of CCFB biomaterials.

2 Experimental study

2.1 Chemicals

Cuttlefish bone (CFB) (*Sepia officinalis* which is commonly found in the Mediterranean Sea and along the Alexandria coast) was purchased from the Governorate of Alexandria, Egypt (Fig. S1), sodium hydroxide (NaOH; purity 98%) was purchased from Scharlau, Barcelona, Spain. Hydrochloric acid (HCl; 37% purity), methanol (HPLC grade, ≥99.9%) was obtained from Merck, Darmstadt, Germany, Bi-distilled water. Cholecalciferol (vitamin D_3) ($C_{27}H_{44}O$) (purity 98%) was purchased from Salvavidas Pharmaceutical Pvt. Ltd., India.

2.2 Preparation of CCFB (calcined cuttlefish bone)

Marine waste cuttlefish bone from *Sepia officinalis* was collected from Alexandria Governorate beach, Alexandria city, Egypt in average 5–8 inches CFB pieces. To mitigate odor and microbial contamination, the CFB underwent initial processing steps. It was excised into smaller fragments and subsequently subjected to a series of treatments. Initially, it was cleansed with deionized water, followed by a ten-minute boiling phase, and then dried at 100 °C for 12 hours.[36] Subsequently, the CFB was pulverized into a powder using a ball mill (photon ball mill).[37] Calcination was then carried out in a muffle furnace for 1 hour at 900 °C. Following calcination, the furnace was allowed to cool to room temperature and finally formed calcined cuttle bone (CCFB). Prior to analytical characterization, the samples were stored in a desiccator.

2.3 Loading process

Firstly, 10 mg of cholecalciferol was dissolved in 10 mL of ethanol (solvent) to obtain a concentration of 1 mg mL^{-1}. In a 50 mL beaker, 1 g of previously prepared CCFB was placed, then the prepared cholecalciferol solution was gradually added to the CCFB under continuous magnetic stirring for 1 hour at room temperature (25 ± 2 °C). The pH of the solution was adjusted to 7 to encourage the loading of cholecalciferol onto the CCFB. The mixture was then filtered to separate any unloaded cholecalciferol from the loaded CCFB. The loaded CCFB was washed with distilled water to remove excess or unbound cholecalciferol. Finally, the cholecalciferol-loaded CCFB was dried in an oven at 40 °C to remove residual solvent and moisture.

2.4 Evaluation of loading efficiency of cholecalciferol on CCFB

Firstly, a standard calibration curve for cholecalciferol was plotted between the absorbance and concentration of cholecalciferol, the absorbance of cholecalciferol was measured using an Evolution 350 UV-Vis Spectrophotometer (Thermo Fisher Scientific, Massachusetts, USA) at wavelength 265 nm which was obtained from wavelength scanning at range 200–400 nm, where at this wavelength, maximum absorbance for cholecalciferol was obtained. Then, transfer 25 mg of the cholecalciferol loaded CCFB to 50 mL of ethanol and subjected to centrifugation at 10 000 rpm for 15 minutes. The supernatant was then analyzed using UV-Vis Spectrophotometer to quantify the amount of cholecalciferol unloaded on CCFB. The loading efficiency was determined by comparing the initial amount of cholecalciferol in the solution to the amount remaining after the loading process using eqn (1) and (2) and the loading efficiency (%) was calculated using eqn (3):

$$\text{Amount of cholecalciferol in solution} = C_{\text{Cholecalciferol}} \times V_{\text{solution}} \tag{1}$$

$$\text{Amount of cholecalciferol loaded} = \text{Initial amount} - \text{Amount remaining in solution} \tag{2}$$

$$\text{Loading Efficiency}(\%) = \frac{\text{Amount of Cholecalciferol Loaded}}{\text{Initial Amount of Cholecalciferol}} \times 100 \tag{3}$$

2.5 Material characterization

Several analytical techniques were employed to characterize (CCFB): the crystallinity of the sample was assessed using a PANalytical (Empyrean) X-ray diffractometer equipped with Cu-Kα radiation (wavelength of 0.154 nm, $I = 35$ mA). Scanning occurred at a rate of 8° min^{-1} within a two-theta range of 5° to 80°. Fourier transform infrared spectroscopy (FTIR): functional groups present in the CCFB were determined using FTIR spectroscopy (Bruker-Vertex 70, KBr pellet technique, Germany) within the spectral range of 400 to 4000 cm^{-1}. Scanning electron microscopy (SEM): the morphology of the CCFB was analyzed using field emission scanning electron microscopy (FESEM) and energy dispersive spectroscopy (EDX). Cholecalciferol concentrations were monitored using an Evolution 350 UV-Vis Spectrophotometer (Thermo Fisher Scientific, Massachusetts, USA). The pH of the solution was measured using an automatic surface pH meter (Adwa–AD1030). The Brunauer–Emmett–Teller (BET) surface area, pore volume, and pore diameter were determined by nitrogen adsorption–desorption isotherms using a TriStar 3020 instrument from Micromeritics, USA. To perform thermogravimetric analysis (TGA), a Japanese Shimadzu DTG-60H apparatus was used. A nitrogen flow of 40 mL min^{-1} was used to heat the material (about 8 mg) from 0 to 500 °C at a rate of 10 °C min^{-1}. JEM 2100 HRT, HIGH RESOLUTION TEM made in JAPAN accelerating voltage = 200kv; resolution = 0.20 nm; high magnification 50 to 6000×, diffraction pattern, indexing for diffraction pattern lattice crystal lattice for crystalline particals inter-planer space by using forier transformation.

2.6 Cytotoxicity and biocompatibility study

2.6.1 Cell culture. Human osteosarcoma (MG-63) cell line (ATCC, USA) was cultured for evaluating the cytotoxic effects of CCFB and cholecalciferol-loaded CCFB. Cells were cultured in DMEM (Thermo Fisher Scientific, China) supplemented with 10% fetal bovine serum (FBS) and 1% penicillin/streptomycin. They were maintained at 37 °C in a humidified atmosphere with 5% CO_2.

2.6.2 MTT assay. For the MTT assay, 1×10^4 cells were plated in each well of a 96-well plate and allowed to incubate overnight. The following day, the culture medium was replaced with fresh medium containing CCFB and CCFB after loading of cholecalciferol at various concentrations (0–500 μg mL^{-1} in triplicate and incubated for about 24 h at 37 °C in a CO_2 incubator. Afterward, the medium was carefully removed, and the wells were washed twice with PBS. The cells were then treated with 10 μL of MTT solution (5 mg mL^{-1}) and incubated for 4 h. Subsequently, 100 μL of DMSO was added to dissolve the formazan crystals, and after 15 min, the absorbance was measured at 570 nm using an M200 Pro microplate reader. Cell viability was calculated as a percentage relative to untreated control cells.

2.6.3 Assessment of biocompatibility of CCFB and cholecalciferol-loaded CCFB on MG-63

2.6.3.1 Preparation of stock solution of each tested formula. A stock solution of 100 μg mL^{-1} was prepared from CCFB and cholecalciferol-loaded CCFB nanoparticles by reconstitution the 0.1 grm in the appropriated volume of 1 mL of DMSO, followed by sonication for 5 seconds, and aliquoted and stored at −20 °C until use. For all experiments, the final concentrations of the test compound were prepared by diluting the stock with the medium. The carrier solvent (0.1% DMSO) was added to the control cells.

2.6.3.2 Treatment of MG-63 by different concentrations of CCFB and cholecalciferol-loaded CCFB nanoparticles for 24 h. One day before conducting the experiment, the Human Osteosarcoma cells (MG-63), cat no: ATCC CRL 1427 cells obtained from American Type Culture Collection (LGC Promochem, UK). The cells were prepared for experiments using the conventional trypsinization procedure with trypsin/EDTA. Cells were seeded in a 96-well culture plate. 8×10^3 cells per well of cells were seeded in 200 μL of Dulbecco's Modified Eagle Medium (DMEM), supplemented with 10% Fetal Bovine serum (FBS), and 1% of penicillin G sodium (10.000 UI), streptomycin (10 mg) and amphotericin B (25 μg) (Gibco, Thermosientific, Germany). Culture plates were incubated at 37 °C in an atmosphere of 5% CO_2 for 24 h to attach cells. On the next day, a constant concentration of serial concentrations of each formula "5, 10, 25, 50, 100, and 500 μg mL^{-1}, were prepared for the treatment of the targeted cancer cells. In addition, the carrier solvent (0.1% DMSO) was used for control cells. Cells were maintained at 37 °C in an atmosphere of 5% CO_2 for 48 h.

2.6.3.3 Staining of cells with trypan blue. After 24 h of treatment with the tested materials, MG-63 cells were subjected to Trypan blue exclusion staining to assess cell viability.[38] The culture medium was aspirated, and cells were washed twice with sterile phosphate-buffered saline (PBS) (Thermo Fisher Scientific, Cat. no. 10010023). Cells were then detached using 0.25% Trypsin-EDTA (Thermo Fisher Scientific, Cat. no. 25200056) and incubated at 37 °C for approximately 3–5 minutes until complete detachment was observed. Trypsin was neutralized with complete DMEM medium containing 10% fetal bovine serum (FBS; Gibco, Cat. no. 26140079), and the cell suspension was collected and centrifuged at 300×*g* for 5 minutes. The resulting pellet was resuspended in 1 mL of sterile PBS. A 10 μL aliquot of the cell suspension was mixed with 10 μL of 0.4% Trypan Blue Stain (Invitrogen™, Thermo Fisher Scientific, Cat. no. T10282) and incubated at room temperature for 3 minutes. The stained cells were observed under a light microscope "LABOMED Fluorescence microscope LX400, cat no: 9126000; USA". Blue-stained cells were considered non-viable, while unstained cells were considered as viable. Cell viability was calculated as the percentage of viable cells out of the total cell count.

2.7 Bacterial strain and growth conditions

The *Staphylococcus aureus* (*S. aureus*) strain was sourced from ATCC (700260) originating from a clinical isolate of human osteomyelitic bone and Methicillin resistant *Staphylococcus aureus* (MRSA) strains ATCC (33592). The stock culture was streaked onto Tryptic Soy Agar (TSA) plates and preserved in glycerol at −80 °C. Bacterial colonies grown on TSA plates were inoculated into 5 mL of Tryptic Soy Broth (TSB) and cultured overnight at 37 °C with aeration. The overnight bacterial cultures were then diluted at a 1 : 5 ratio and incubated for an additional 2 h with shaking at 200 rpm until reaching mid-log phase, as indicated by an optical density (O.D.) of 0.5 at 600 nm, corresponding to approximately 5×10^7 CFU mL^{-1} (for *S. aureus*) and 3×10^7 CFU mL^{-1} (for MRSA). Cells were collected by centrifugation at 4300×*g* for 20 min, and the pellet was rinsed with PBS. Before conducting the antimicrobial test, a growth curve of *S. aureus* as well as MRSA in DMEM: F12 cell culture medium was established by inoculating 1×10^6 CFU ml^{-1} *S. aureus* and 0.5×10^6 CFU mL^{-1} cells into 1 mL of DMEM with 10% fetal calf serum and 2 mM L-glutamine in 1.5 mL Eppendorf tubes, incubated at 37 °C with shaking at 220 rpm. Absorbance was measured every 30 min at a wavelength of 600 nm, resulting in a sigmoidal growth curve that demonstrated the feasibility of cultivating *S. aureus* in DMEM cell culture medium. Previous studies have examined *S. aureus* co-culture with host cells and its growth in animal cell culture media.[39]

2.7.1 Antimicrobial assay. The antimicrobial assay was conducted in 1.5 mL Eppendorf tubes containing 5×10^7 CFUs mL^{-1} of *S. aureus* and 3×10^7 CFU mL^{-1} MRSA in 1 mL of (DMEM)/Ham's F12 medium (DMEM/F12; Sigma USA). The medium was supplemented with 10% FBS and 2 mM L-glutamine. The assay was performed in triplicate, following a procedure similar to the macro-dilution method for antimicrobial testing. Various concentrations of CCFB and CCFB after loading of cholecalciferol, ranging from 1 to 5 μg mL^{-1}, were added to the tubes. Vancomycin (1–5 μg mL^{-1}) was included as a positive control in all antimicrobial assays to benchmark the efficacy of the tested materials against a clinically relevant antibiotic. The tubes were sealed and placed in a dry incubator with shaking at 220 rpm at a temperature of 37 °C. Incubation times were set at intervals of 1, 2, 3, 4, 5, or 6 h. After incubation, the *S. aureus* and MRSA cells were collected by centrifugation at 4000×*g*, and the pellet was resuspended in PBS buffer. Serial dilutions were prepared, and 100 μL samples were plated on TSA plates. CFUs were counted following overnight incubation.[40]

2.7.2 Zone of inhibition (Kirby–Bauer disk diffusion assay). Mueller–Hinton Agar (MHA) plates (90 mm diameter) were prepared according to the manufacturer's instructions and allowed to solidify, after which a standardized bacterial suspensions were evenly inoculated onto the entire surface of each plate using a sterile cotton swab, swabbing in three directions with plate rotation to ensure uniform distribution; the inoculated plates were then left to dry at room temperature for 15 min before the application of sterile paper discs (6 mm diameter) impregnated with 10 μL of the test compounds (CCFB and CCFB loaded with cholecalciferol) at concentrations of 1, 2, 3, 4, and 5 μg mL^{-1}, alongside negative control discs (sterile solvent) and positive control disks (vancomycin, 5 μg mL^{-1}), which were aseptically placed on the agar surface with adequate spacing to prevent overlapping zones and gently pressed for full contact; the plates were subsequently inverted and incubated at 37 °C for 18–24 hours, after which the diameter of the clear zone of inhibition around each disc was measured to the nearest millimeter using a ruler or zone reader, with measurements taken from the back of the plate against a dark background, and all experiments performed in triplicate with mean inhibition zone diameters recorded for each compound and concentration.

2.8 Oxidative stress measurement assays

Osteoblast cells were cultured in a T-25 flask as previously described. Various concentrations of CCFB and CCFB after loading of cholecalciferol (5, 10, or 15 μg mL^{-1}) were introduced and incubated for 24 h. After the incubation with CCFB and CCFB after loading of cholecalciferol, the cells were rinsed with PBS buffer at pH 7.4 and then lysed using a cold lysis buffer at pH 8.8, which contained 50 mM Tris and 1 mM EDTA, along with a protease inhibitor (P8340). A cell disruptor facilitated rapid cell lysis. The resulting cell lysate was transferred to an Eppendorf tube and centrifuged at 10 000×*g* for 10 min in a cold centrifuge; the supernatant was then collected for glutathione assay, catalase activity, and carbonyl content analysis. The total protein concentration in the supernatant was determined using the BCA assay (23227), following the manufacturer's instructions. In summary, reagents A and B were combined in a 50 : 1 ratio, and 180 μL of this mixture was added to either 20 μL of the sample or dilutions from the standard curve. The plate was covered and incubated for 30 minutes, after which absorbance was measured at 562 nm using a UV-Vis Bio-tek absorbance Plate Reader.

2.8.1 Glutathione assay. Reduced glutathione levels were determined using a biochemical assay as described in ref. 41, utilizing the cytosolic fraction of cell extracts. Reduced glutathione (GSH, G6013) and 5,5-dithio-bis-(2-nitrobenzoic acid) (DTNB) were prepared in Tris EDTA buffer at a concentration of 2.5 mM each. Standard curves were generated by adding 100 μL of 2.5 mM GSH to a 96-well plate, followed by serial dilutions and the addition of 100 μL of 2.5 mM DTNB reagent to each well. The plate was incubated in the dark for 5 min, after which absorbance was measured at 405 nm to create the standard curve. Similarly, 100 μL of the cytosolic fraction from treated or untreated cells was added to a 96-well plate, followed by 100 μL of 2.5 mM DTNB reagent. After a 5 minute incubation in the dark, absorbance was measured at 405 nm, and the concentration of reduced glutathione was calculated using the standard curve, expressed as nmoles per mg of total protein.

2.8.2 Protein carbonyl and catalase assay. The protein carbonyl content and catalase activity were assessed using specific kits, with numbers 10005020 and 707002, respectively. Both kits were utilized according to the instructions provided by the manufacturer.

2.8.3 Super oxide dismutase assay. The superoxide dismutase (SOD) assay was conducted following the manufacturer's protocol (706002). Osteoblast cells were cultured in a T-25 flask until reaching 70% confluency. Fresh media were added, and cells were treated with nanoparticle concentrations ranging from 5 to 20 $\mu g\ mL^{-1}$, then incubated for 24 h. After incubation, cells were gently harvested using a rubber policeman and homogenized in the manufacturer-recommended buffer (20 mM HEPES buffer, pH 7.2, containing 1 mM EGTA, 210 mM mannitol, and 70 mM sucrose). A standard curve was generated and cellular superoxide dismutase levels were calculated by strictly following the instructions provided in the assay kit manual.

2.8.4 LDH assay. The LDH cytotoxicity assessment utilized Promega's CytoTox-ONE kit (G7890), where osteoblasts were cultured in 96-well plates at 15 000 cells per well and exposed to nanoparticles (1–20 $\mu g\ mL^{-1}$) in 100 μL phenol-free media for 24 h at 37 °C in a CO_2 incubator. After equilibrating the assay components and cell plate to room temperature (22 °C) for 20–30 min, 100 μL of Cytotoxic-ONE reagent was added to each well, with positive control wells receiving 2 μL of lysis buffer for maximum LDH release. Following a 20 minute room temperature incubation, 50 μL of stop solution was added to each well, and the plate was shaken for 10 s before measuring fluorescence (560 nm excitation/590 nm emission) using a Bio-Tek Synergy-2 fluorometer, with background fluorescence from blank media subtracted from all readings to determine the final toxicity percentage, eqn (4).

$$\%\ \text{Toxicity} = (\text{LDH}_{\text{lysed}} - \text{LDH}_{\text{exposed}}) \div (\text{LDH}_{\text{lysed}} - \text{LDH}_{\text{control}}) \times 100 \tag{4}$$

2.9 *In vitro* release study

The *in vitro* drug release of cholecalciferol loaded on the surface of CCFB was evaluated using the dialysis bag method to simulate controlled drug release. Firstly, the dialysis bags were soaked in the dissolution (release) medium overnight. Then, 50 mg of loaded cholecalciferol on CCFB and free cholecalciferol (as a control) were placed in dialysis bags made of cellulose membrane (molecular weight cut-off of 14 000 Da, SERAVA Electrophoresis) that were sealed at both ends with thermo-resistant thread. These bags were immersed in a glass jar containing 900 mL of 0.1 N HCL (pH 1.2, at 37 °C ± 0.5 °C) to simulate the acidic environment of the stomach.[42] The jar was then placed in a shaker incubator (Labsol, India), and it was set at 50 rpm. At predefined time intervals (0.083 h, 0.25 h, 0.5 h, 1 h, 2 h, 4 h, 6 h, 8 h, 12 h, 24 h, and 36 h), 5 mL of the medium surrounding the dialysis bag was withdrawn and replaced with an equal volume of fresh medium to maintain sink conditions. Each sample was filtered through a 0.22 μm nylon syringe filter to remove any nanoparticles that might have passed through the dialysis bag. The concentration of cholecalciferol released into the surrounding medium was measured using an Evolution 350 UV-Vis Spectrophotometer (Thermo Fisher Scientific, Massachusetts, USA) at wave length 265 nm which was chosen after spectrum scanning from 200–400 nm exhibiting the maximum absorbance at this wavelength. The cumulative drug release percentage was calculated by plotting the concentration of released cholecalciferol against time, allowing for an evaluation of the release profile of the loaded cholecalciferol from CCFB compared to the free drug. This method provides a reliable imagination for studying sustained-release profiles.[43–45] The dialysis bag technique, with its efficient diffusion-based release mechanism, is ideal for studying the release of drug-loaded nanoparticles and is particularly advantageous for overcoming drug resistance.[46,47]

Drug release at time t, cumulative drug release (%) were calculated using eqn (5) and (6):

$$\text{Released Drug at time } t = C_t \times V \tag{5}$$

where, C_t represents the drug concentration at time t ($mg\ mL^{-1}$), V represents volume of the dissolution medium (mL).

$$\text{Cumulative drug release}(\%) = \frac{\text{Released drug at time}}{\text{initial amount of drug loaded}} \times 100 \tag{6}$$

2.10 *In vitro* release kinetics

Various release kinetics models were applied including zero-order kinetics (constant release rate), First-order kinetics (release rate depends on the amount of drug remaining), Korsmeyer–Peppas model (power law), Higuchi model (diffusion-controlled release) to give insight into the release mechanism either through diffusion, swelling, or erosion of the loaded formulation (cholecalciferol loaded on CCFB) using the following equations:

$$\text{Zero-order-kinetics } M_t = M_0 + Kt \tag{7}$$

$$\text{First-order-kinetics } \frac{M_t}{M_0} = 1 - e^{-k_1 t} \tag{8}$$

$$\text{Korsmeyer} - \text{Peppas-Model } \frac{M_t}{M_0} = Kt^n \tag{9}$$

$$\text{Higuchi model } M_t = K_\mathrm{H}\sqrt{t} \tag{10}$$

M_t = amount of drug released at time t, M_0 = initial amount of drug, k_1 = first-order rate constant, n is the release exponent that indicates the release mechanism, t = time, k_H = Higuchi rate constant (depends on properties like the diffusion coefficient, solubility, and surface area).

2.11 Statistical analysis

All experiments were performed in triplicate ($n = 3$) unless otherwise specified. Data are presented as mean ± standard deviation (SD). Statistical significance between two groups was assessed using Student's *t*-test. For comparisons among more than two groups, one-way ANOVA followed by Tukey's post hoc test was used. For drug release kinetics, model fitting was performed by non-linear regression and goodness-of-fit was evaluated using the coefficient of determination (R^2). A *p*-value of <0.05 was considered statistically significant.

3 Results and discussion

3.1 Characterization of CCFB and CCFB after the loading of cholecalciferol

3.1.1 Morphological analysis

3.1.1.1 SEM. To assess the morphological alterations induced by heat treatment, the CCFB underwent scrutiny *via* scanning electron microscopy (SEM) (Fig. 1a–f).

They measured 600–750 nm in width.The spherical forms presented and distributed in the images are related to the CaO and MgO.[49,50] At higher magnification, as shown in Fig. 1d–f, particulates or granules with different sizes and surface characteristics may be seen as calcium phosphate.[49,51,52]

3.1.1.2 Topography mapping. 3D topography mapping of CCFB highlight nanoparticle clusters interspersed with holes (Fig. 2a–h) and prominent surface roughness in Fig. 2e. SEM analysis showed that the sample takes the shape of a tulip flower with smooth, parallel longitudinal ridges interspersed with parallel protrusions, as highlighted by the red lines in Fig. 2b. Although the material is relatively larger than its predecessor, small holes were observed within the material, marked by yellow dotted circles. In additinal, the 3D topography mapping in Fig. 2f where the orange and purple lines in the shape harmonize, confirming the zigzag section, and the expansion of the surface roughness. Fig. 2c had a significant modification of irregular structure, suggesting the effectiveness of CCFB loaded with the interaction of the building factor. This is confirmed by the gradation and distribution of colors between surfaces, the 3D topography mapping in Fig. 2e–h, in addition to more roughness due to the preparation steps in Fig. 3(a–d).

3.1.1.3 EDX spectrum. The chemical composition of CCFB was identified using the EDX spectrum. According to the results, the CCFB powder spectrum (Fig. 4a) showed peaks for carbon (C), oxygen (O), magnesium (Mg), calcium (Ca), phosphorus (P), zirconium (Zr), iodine(I), and titanium (Ti). While the presence of these elements, particularly Zr, I, and Ti, is not typically expected in cuttlebone, it could be attributed to in the CFB source environment. Also, the composirion of the element by atomic and weight percent are shown clearly in Fig. 4b. Also, to confirm the composition we used atomic absorption spectrophotometer analysis techniqe by digesting the prepared material through a concentrated hydrochloric acid (HCl), the digested solutions were analyzed for calcium and magnesium contents by atomic absorption spectrophotometer analysis, and the results were 0.434 mg g^{-1} for Ca^{2+} and 0.119 for Mg^{2+}. The EDX and the atomic absorption spectrophotometer analysis results, in conjunction with the SEM (Fig. 4c) and BET analysis and its pore geometry, provide strong evidence the surface of CCFB, resulting a material with enhanced loading properties.

3.1.1.4 SEM loaded sample. SEM images (Fig. 5a–e) revealed the morphological of CCFB in loaded form by cholecalciferol. The presented images show that the pores were more homogeneous in shape and size and well-ordered before adding cholecalciferol. The cholecalciferol-containing CCBF showed irregular pores and distorted walls, which could be affected by the loading method on the structure and properties of the loaded sample. In addition, the smaller pores with closer walls lead to a more packed structure in loaded CCBF which verify the lower porosity and a high packed structure can be the result of the formation of H bond between cholecalciferol and CCBF nanoparticles.[53]

3.1.1.5 TEM loaded sample. High resolution transmission electron microscopy (HRTEM) micrographs of calcinated cattle fish bone reveal important details about its ultrastructure. CCFB typically shows a mineral matrix where the organic contain is mostly removed (Fig. 6a). These crystals often appear as layered elongated, plate-like structures. HRTEM images show these mineral structures arranged in clusters or lanes spanning tens of nanometers (Fig. 6a). The calcination process increases the crystallinity and size of CCFB crystals as organic content is burned off, enhancing the bone's rigidity. Calcined bone micrographs also reveal polycrystalline mineral clusters and clear separation between mineral and carbon based-derived void spaces. This detailed ultrastructural information helps us understand material mechanical properties and guides biomaterial and biomedical applications. As shown in loaded material indicates differences in particle size and orientation, with a consistently rough surface exhibiting a highly porous structure. The structure prominently features rod-shaped nanoparticles clustered together, forming two-dimensional rod-like aggregates, which further develop into layered formations, creating a three-dimensional architecture within the CCFB. The integration of VD onto the surface (CCFB) leads to their incorporation either within the gaps of the CCFB structure or as a coating enveloping the CCBF matrix. These alterations in

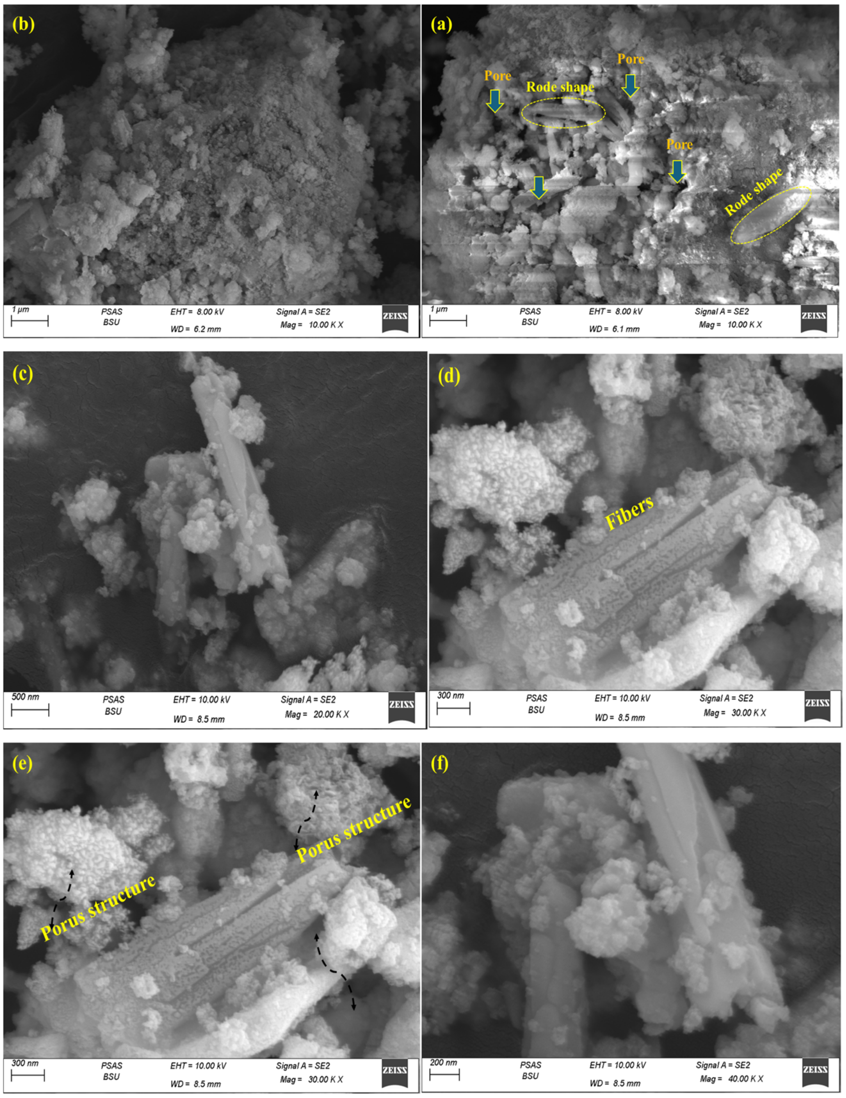

Fig. 1 (a–f) Show the SEM images of the CCFB material at different magnifications. Rode structures of CCFB that were not completely calcined are visible in the SEM images.[48]

texture contribute to a substantial elevation in surface roughness, yielding a more heterogeneous topography and an improvement in the total composite's porosity, as shown in Fig. 6b. As a result, this improvement is likely to affect the biochemical behavior and overall surface area of the composite, increasing its efficacy for medicinal uses and enhance the composite's effectiveness in bone remediation and biomedical applications.

3.1.1.6 3D characterization for the CCFB and loaded sample. Surface morphology has been extensively studied because it can display vital properties, including deformations and heterogeneities that can affect the material's application. Using image J software was used to analyze the topographic HRTEM image (Fig. S2 a and b). The two samples have a distinct height distribution. The surface texture directions of the samples were analyzed (Fig. S3), as well as the related values of surface texture parameters, which may be associated with the inhomogeneity of the surface.[54] Table S2 shows the surface parameters in terms of roughness (Ra), roughness skewness (Rsk), roughness kurtosis (Rku). The kurtosis and skewness parameters are processed using the square root of the surface height distribution (RMS). Roughness kurtosis (Rku) is a measure of the "sharpness" of a surface and the unpredictability of profile heights. Spiky surfaces have $Rku > 3$, bumpy surfaces have $Rku < 3$, and absolutely random surfaces have $Rku = 3$. Accordingly, the values of Rku are 16.58 and 33.36 for CCFB, and Loaded sample, respectively, which indicates the two prepared samples have a rough surface. A roughness skewness (Rsk) value reflects the symmetry of the surface; a negative value implies a predominance of valleys, while a positive value indicates a "peaky" surface. The two materials have a negative value, indicating that the surface of them are a valley surface.[55] Fig. S2 showed the Waviness and Roughness of the prepared materials.

3.1.2 Textural properties. The specific surface area (BET), pore volume, and pore diameter of the CFB and CCFB were assessed through N_2 adsorption–desorption isotherms

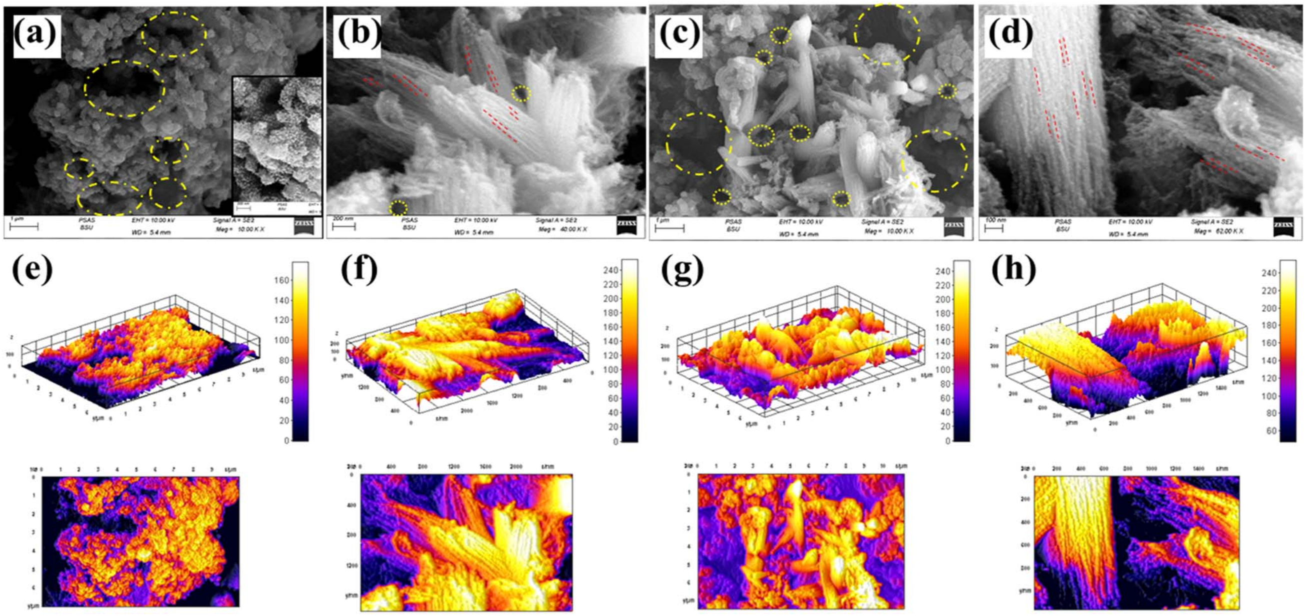

Fig. 2 (a–h): SEM micrographs of (a) CCFB, (b) lamellar wall, (c) CCFB loaded cholecalciferol, and (d) CCFB loaded cholecalciferol magnifications. 3D topography mapping of (e) CCFB, (f) lamellar wall, (g) CCFB loaded cholecalciferol, and (h) CCFB loaded cholecalciferol magnifications.

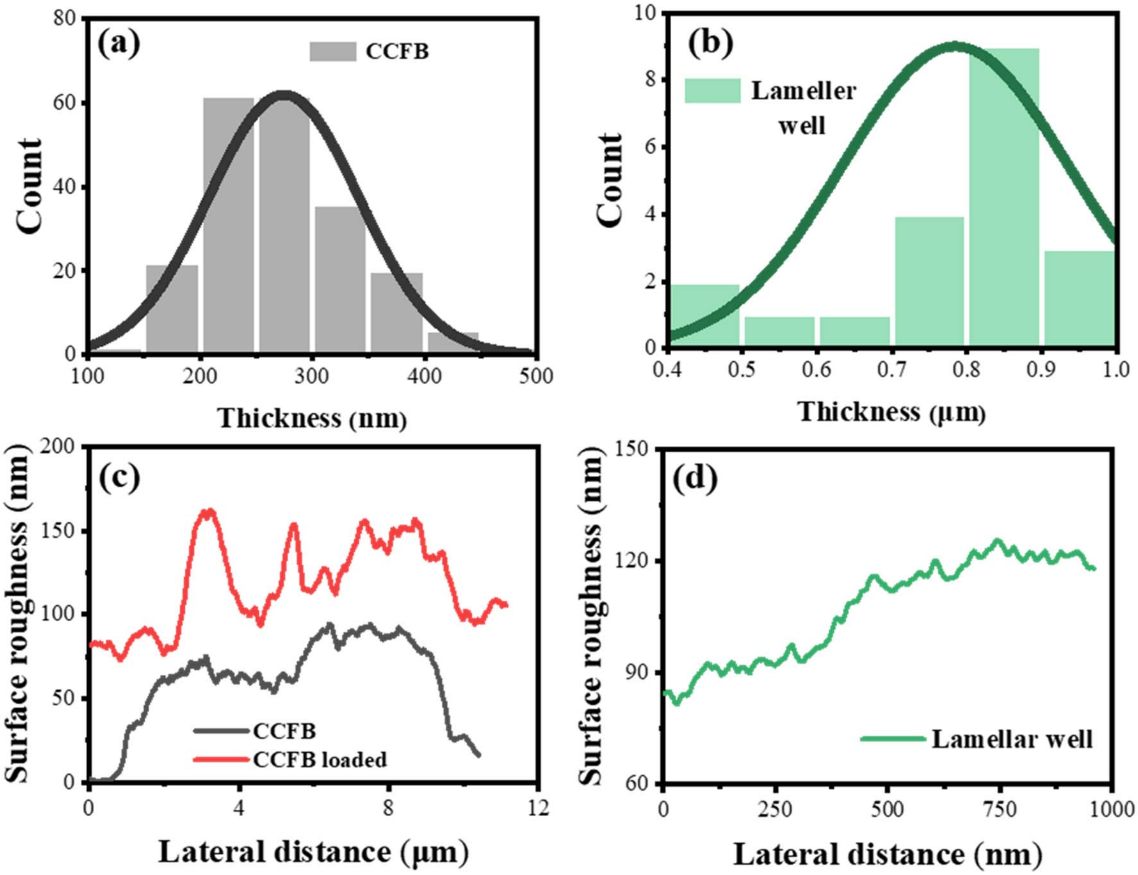

Fig. 3 (a–d): Surface roughness of (a) CCFB, and CCFB loaded cholecalciferol in microscale and (b) lamellar wall in nanoscale. Thickness distribution of (c) cholecalciferol and (d) CCFB.

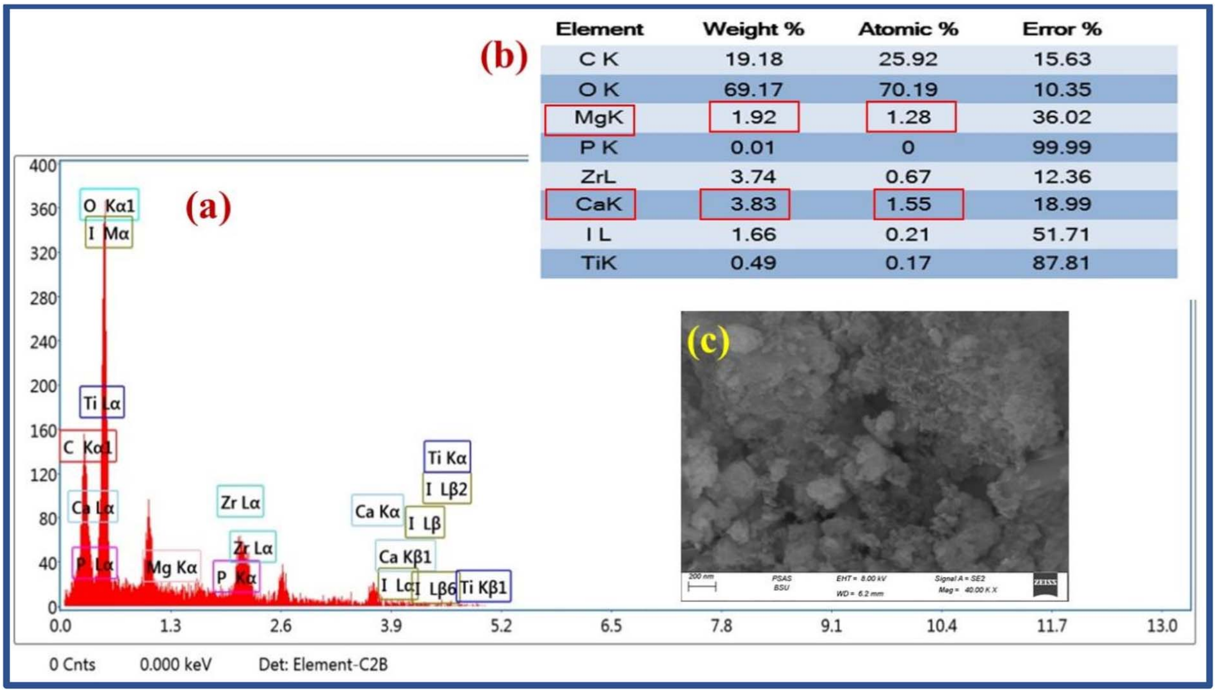

Element	Weight %	Atomic %	Error %
C K	19.18	25.92	15.63
O K	69.17	70.19	10.35
MgK	1.92	1.28	36.02
P K	0.01	0	99.99
ZrL	3.74	0.67	12.36
CaK	3.83	1.55	18.99
I L	1.66	0.21	51.71
TiK	0.49	0.17	87.81

Fig. 4 (a–c): (a) EDX of the CCFB and the inset figure (b) refers to the elemental composition percent and (c) SEM micrographs of CCFB at 900 °C.

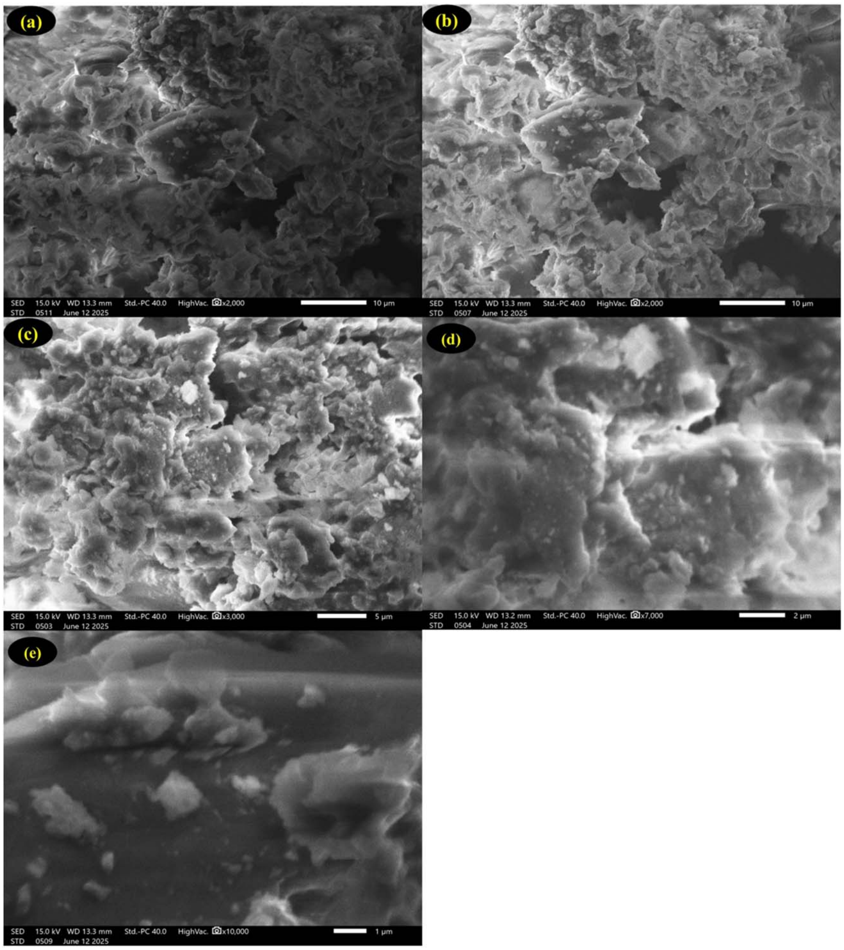

Fig. 5 (a–e): SEM images of the prepared CCFB loaded cholecalciferol with different magnifications.

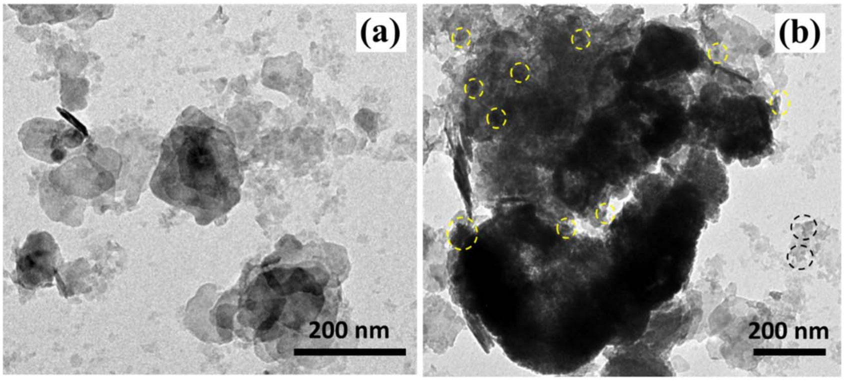

Fig. 6 The HRTEM images of (a) CCFB, and (b) CCFB material loaded by cholecalciferol.

Table 1 Surface parameters of the CFB and CCFB

Item	CFB	CCFB
BET surface area ($m^2\ g^{-1}$)	370.00	92.64
Total volume in pores ($cm^3\ g^{-1}$)	0.6156	0.16
Pore diameter (nm)	6.69	5.70

conducted at 77 K. In accordance with the International Union of Pure and Applied Chemistry (IUPAC) classification, Fig. 6 displays the constructed CBF and CCFB N2 gas adsorption-desorption. These parameters influence the adsorption behavior of the synthesized materials by measuring its surface area, mesoporosity, and average pore size. The isotherm of the adsorbent of type V is associated with the back loop of H4 and H3 type occurs when the drug, particularly the monolayer, interacts instead of the sample's surface, according to the IUPAC classification. This attitude can be caused by the creation of a weak bulk of plate-like shape particles or the clustering of crack-shaped pores.

The BET surface area of the prepared materials and mean pore diameter and pore volume was presented in Table 1. As illustrated in (Fig. 7a–d). Also, the pore size distribution (PSD) curves was presented inset Fig. 7(b and d). CFB exhibits a relatively high BET surface area of 370 $m^2\ g^{-1}$, with a total pore volume of 0.615 $cm^3\ g^{-1}$. While calcination reduces surface, it increases the number of active Ca^{2+}/PO_4^{3-} sites on the surface of CCFB. These sites are responsible for loading propriety. Also, we notice that the pores shrink, but the chemically active surface becomes cleaner and more effective.We prefer CCFB because it is pure, stable, biocompatible, and has controlled surface chemistry. Although raw CFB powder exhibits a comparatively higher surface area, the calcined form is generally preferred for practical applications. Calcination removes residual organics such as collagen, fats, and proteins, yielding a phase-pure CCFB structure. This process not only eliminates impurities and microbial susceptibility but also enhances chemical and structural stability in aqueous media. Moreover, the exposure of active Ca^{2+} and PO_4^{3-} surface sites after calcination facilitates ion exchange and adsorption, making the material more effective despite its lower surface area. Therefore, the calcined cattle bone powder is favored over the untreated form due to its purity, stability, and well-defined surface chemistry, which are critical for both environmental and biomedical applications.[56]

3.1.3 X-ray diffraction (XRD). The raw CFB sample's XRD (Fig. 8a) shows that aragonite makes up the whole inorganic matrix. Halite 31.7° traces were also found, most likely from seawater. Also, sharp peaks of aragonite $CaCO_3$ can be seen in the spectrum of CCB at 2 theta 28.9°, 34.3°, 36.0°, 29.5°, 31.9°, 47°, 51.5° and 54°. Which confirm the fact that aragonite makes up the majority of CFB.[57,58] B-chitin could account for the low intensity peaks at 10–25.[59]

As shown in Fig. 8b, CCFB that calcined at 900 °C has a high peak intensity of the diffraction peak at degrees of peak Miller index at (113), (116), (300), (012), (112), (048), (023), (223), (114) at degrees of 18.3°, 23.13°, 29.47°, 34.17°, 36.07°, 43.3°, 51°, 65.65°, 70° respectively. The calcination of CFB at 900 °C for 5 hours resulted in the formation of a new calcium oxide (CaO) phase derived from aragonite mineral, which was characterized by distinct peaks at 32°, 40°, 54.2°, and 64.6°.[60] Additionally, the crystalline structure of MgO, which may be derived from dolomite (CaMg (CO_3)) or magnesite ($MgCO_3$) minerals associated with CFB, exhibits peaks at $2\theta = 37°$, 43.3° 62.4°∘, 78.7°, 74.8°.[61,62]

The X-ray diffractograms of loaded sample is shown in Fig. 8c as observed, in the loaded sample that a slightly moved to the left with decreasing in the intensity of the appeared peak which related to presence of cholecalciferol interacted with the surface of CCFB NPs. However, the characteristic peaks of cholecalciferol were not observed, suggesting that the cholecalciferol was confirming the interaction when incorporated into CCFB. Similar observation was found by Pantić *et al.*[63] for supercritical impregnation of fat-soluble vitamins into alginate aerogels. These authors also showed the amorphous state of the loaded drug.

3.1.4 FT-IR analysis. CCFB's FT-IR spectrum is shown in Fig. 9a. Because water molecules stretch, CCFB showed modest OH and NH group absorption peaks in the 3651–3445 cm^{-1} region.[27,64] Carbonate groups n1 (out-of-plane bend), n2 (doublet C–O in plane bend), and n4 (aragonite structure) are identified by strong peaks at 1128, 885, and 702 cm^{-1},

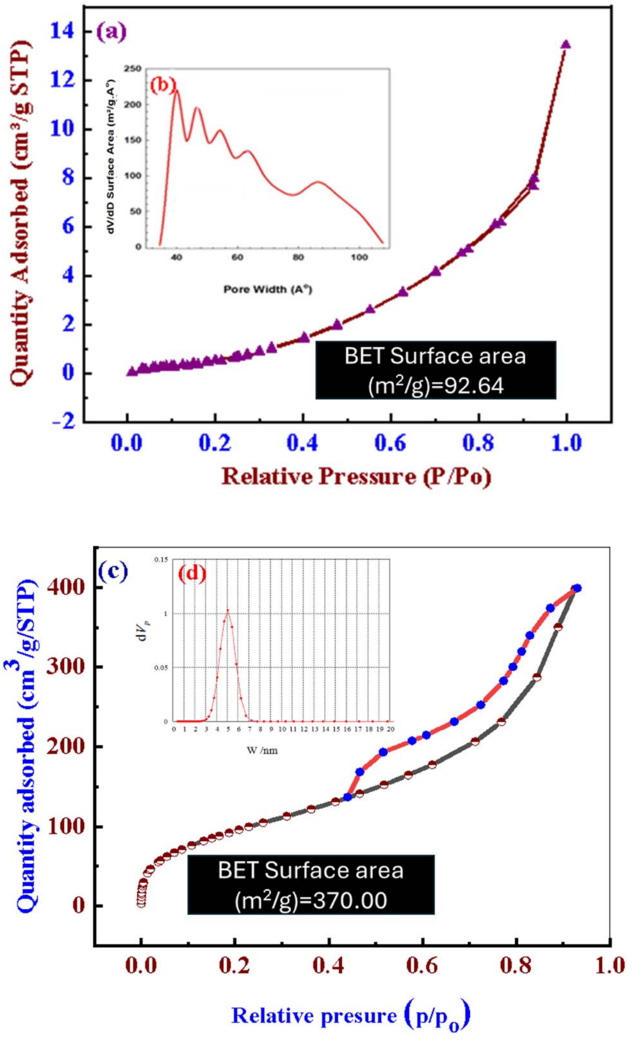

Fig. 7 (a and c) Adsorption–desorption isotherms of N_2 at 77 K and (b and d) pore size distribution curves for the CFB and CCFB respectively.

respectively.[65] The n3-asymmetric stretch of the aragonite carbonate structure was confirmed by a wide peak located around 1441 cm^{-1}.[66,67] After Loading of cholecalciferol, the FTIR spectra can provide valuable information on potential interactions between cholecalciferol and CCFB. As shown in Fig. 9b the distinctive FTIR bands following cholecalciferol loading. With a few modifications, CCFB following cholecalciferol loading displayed the same distinctive bands as CCFB prior to cholecalciferol loading as pure Cholecalciferol showed the characteristic peak at 3421 cm^{-1} is attributed to the hydroxyl groups corresponding to the O–H stretch. Another absorption band 2928 cm^{-1} corresponds to C–H aliphatic stretch, band 1629 cm^{-1} corresponds to C=C of benzene ring of cholecalciferol stretching vibration, 1409 cm^{-1} indicates the methylene C–H stretching vibrations, 870 cm^{-1} correspond to the C–H and C–O stretching vibrations, respectively.[68] Also, the loading was confirmed by shift which was shown after loading as the following: (i) the peak at 3445 cm^{-1} in CCFB before loading changed to 3221 cm^{-1} with a broader and more intense pattern, while the O–H peak at 3651 cm^{-1} for CCFB before loading shifted to 3421 cm^{-1} and became broader, this approve the integration of the cholecalciferol in the pores of the CCFB. (ii) The presence of an interaction between the CCFB and cholecalciferol may be indicated by the fact that the peaks at 1441 cm^{-1} and 1409 cm^{-1} shifted to become sharper and more intense. (iii) the peak at 1128 cm^{-1} shifted to 1109 cm^{-1} and became more broader, and the peaks at 885 and 702 cm^{-1} shifted to 873 and 676 cm^{-1}, respectively, became more intense and broader. Fig. 9a and b, the FTIR investigations concerned the intramolecular H-bonding among the CCBF and cholecalciferol. The hydrogen bonding intensity was calculated from the ratio of the absorbance bands at 3420 and 3437 cm^{-1} (for the–

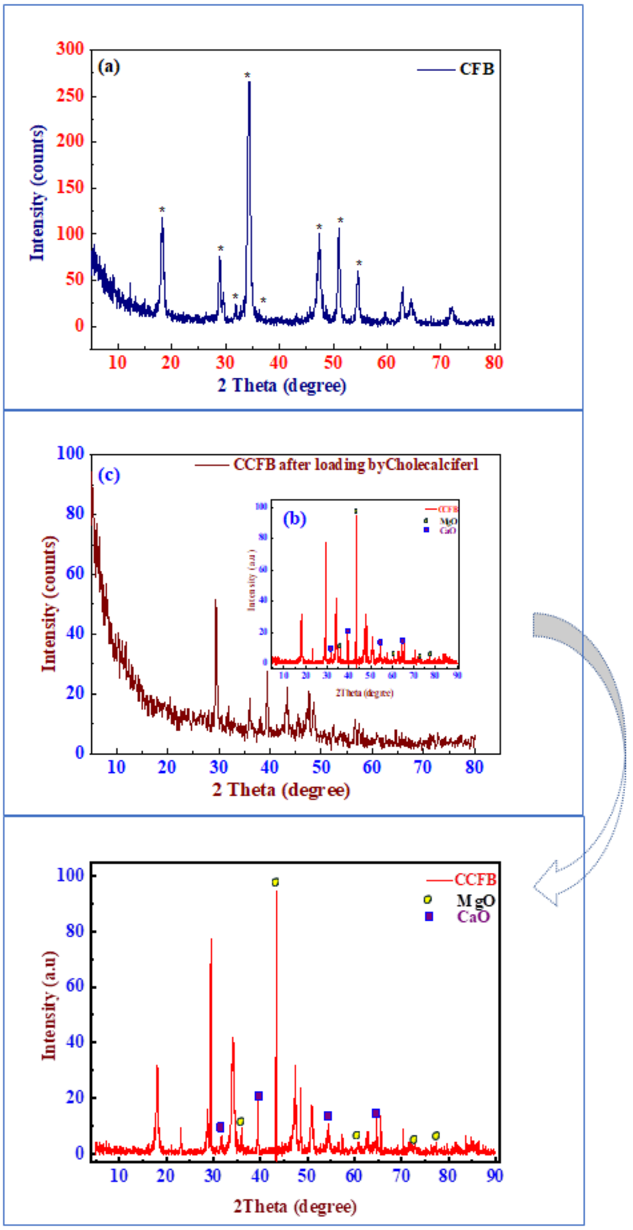

Fig. 8 (a and b): (a) XRD patterns of the CCB, (b) inset figure of CCFB after loading by cholecalciferol and (c) CCFB.

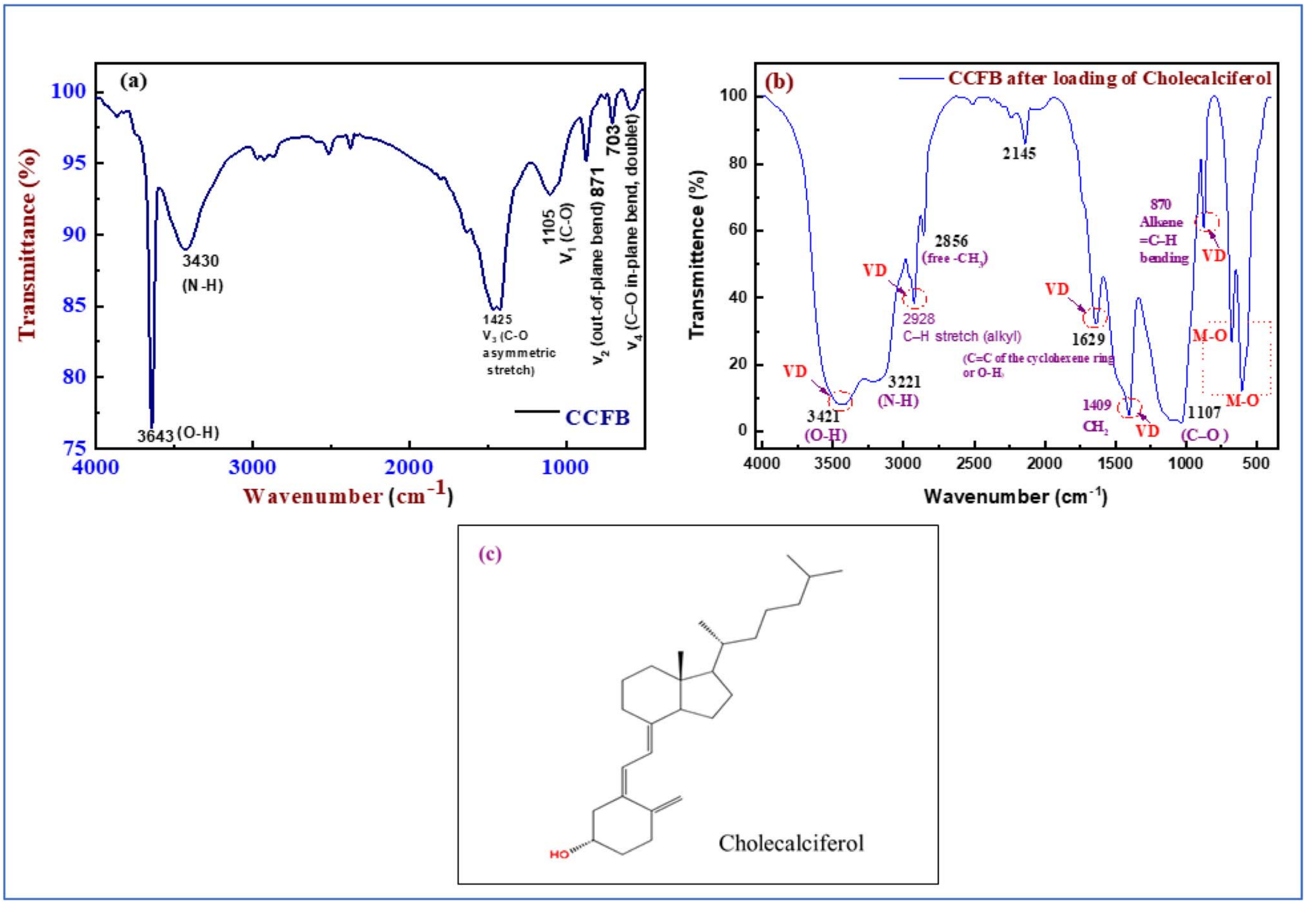

Fig. 9 (a–c): FTIR spectrum of the CCFB (a) before loading cholecalciferol, (b) after loading of cholecalciferol, and (c) chemical structure of the loaded drug.

OH peak) and 1636 and 1640 cm^{-1}(for the C–O peak) in CCFB and CCFB/cholecalciferol, respectively, showing a significant increase in the case of the CCFB/cholecalciferol nanocomposite (3.995) compared to that of CCFB (1.01), concerning the H-bonding interactions between the CCFB and cholecalciferol Through FTIR investigations, which confirmed the successful loading of cholecalciferol onto the CCFB surface[24] (Fig. 9c).

3.1.5 Thermo gravimetric analysis (TGA/DTG).

The thermal analysis graph of CCFB shows a Thermogravimetric (TG) curve in red and its derivative (DTG) in blue plotted against temperature in °C. Initial Stability to ∼400 °C, the TG curve remains near 100%, indicating no significant mass loss (Fig. 10). This means the CCFB is thermally stable up to about 400 °C. First mass loss from ∼400 °C to ∼500 °C where TG decreases sharply from about 100% to ∼80%. The corresponding DTG shows a strong negative peak here, indicating a rapid mass loss phase. This is likely due to the decomposition or loss of organic residues or carbonate components remaining in the bone. As shown in Fig. 10a plateau start from ∼500 °C to ∼750 °C. The TG curve levels off near 80–75%, indicating relative thermal stability after the first decomposition step. The second mass loss start ∼750 °C to ∼850 °C. This secondary decomposition could be related to further breakdown of carbonates or other inorganic compounds. The final Plateau above 850 °C. TG stabilizes near 70%, indicating the residual stable inorganic material, such as metal oxides formation. This analysis reveals the thermal stability and decomposition behavior critical for applications in biomaterial.

In contrast, the TGA curve for the CCFB/cholecalciferol-loaded (Fig. 10) exhibits a distinct weight loss event of approximately 8.5% between 200 °C and 400 °C, with a peak decomposition temperature (from DTG) around 450 °C. This mass loss is unequivocally attributed to the thermal degradation and combustion of the loaded cholecalciferol molecules.[69,70] The absence of this feature in the pure CCFB sample provides direct evidence for the successful physical adsorption and incorporation of cholecalciferol into the porous CCFB structure. The mass loss peak near 46 °C in both the TG and heat flow curves likely corresponds to the loss of physically adsorbed water or moisture from the calcined cattle bone loaded with cholecalciferol. This relatively low-temperature event is typical for evaporation of surface or loosely bound water molecules, which does not involve decomposition of major components. Such moisture loss usually causes a small weight decrease and an endothermic peak in the heat flow curve as heat is absorbed to evaporate water.The decomposition temperature of cholecalciferol within the CCFB matrix (∼450 °C) is significantly higher than the melting point of pure crystalline cholecalciferol (83–86 °C),[71]

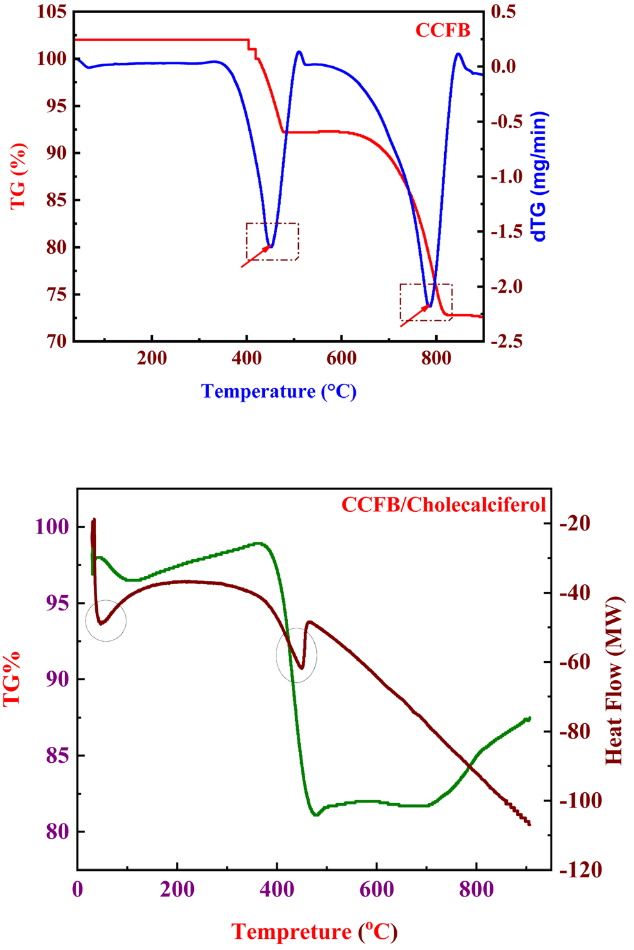

Fig. 10 TGA/DTG thermograms of CCFB and loaded one.

suggesting that the interaction with the CCFB surface and confinement within its pores enhances its thermal stability. This high decomposition temperature indicates that the CCFB/cholecalciferol composite is highly stable under normal storage and physiological conditions, ensuring the integrity of the loaded drug during potential sterilization processes (*e.g.*, gamma irradiation) and throughout its intended biomedical application.

3.1.6 Proposed mechanism of cholecalciferol-CCFB interaction and release. The interaction between CCFB and cholecalciferol is primarily driven by physical adsorption and potential hydrogen bonding, facilitated by the high surface area and porosity of CCFB as confirmed by BET analysis, which provides ample adsorption sites on the calcium carbonate matrix. FTIR analysis indicates that cholecalciferol interacts with surface –OH groups and Ca^{2+} ions through weak hydrogen bonds and van der Waals forces, enabling efficient, non-covalent loading while preserving its bioactivity. In aqueous environments, the porous CCFB structure supports gradual diffusion of cholecalciferol, resulting in a sustained release profile influenced by the molecule's surface affinity and the matrix's dissolution rate. This controlled release ensures prolonged therapeutic availability, while the release of calcium ions may synergistically promote bone health and cellular functions. Together, these effects enhance the antimicrobial and antioxidant performance observed in the study. A schematic illustration of this mechanism is provided in Fig. S4, depicting the adsorption, retention, and controlled release behavior of cholecalciferol from the CCFB carrier.

3.2 Cell viability and biocompatibility analysis

As shown in Fig. 11, both materials exhibited high cell viability (>95%) at low concentrations (5, 10, and 25 μg mL^{-1}), indicating minimal cytotoxicity. Moderate reductions were observed at 50 and 100 μg mL^{-1}, with viability remaining above 80%. At the highest concentration of 500 μg mL^{-1}, a more pronounced decrease in cell viability was recorded that was approximately 70.4% for CCFB and 75.2% for cholecalciferol-loaded CCFB. The high cell viability observed across a wide concentration range (5–100 μg mL^{-1}) provides strong evidence for the biocompatibility of both CCFB and cholecalciferol-loaded CCFB materials. These quantitative viability assessments indicate that the materials do not release toxic components and are well-tolerated by mammalian cells *in vitro*. Statistical analysis using one-way ANOVA followed by Tukey's post hoc test confirmed that the difference in cell viability at 500 μg mL^{-1} between CCFB and cholecalciferol-loaded CCFB was statistically significant ($p < 0.05$), while all other concentrations showed no significant difference ($p > 0.05$) (Table S3). The exhibited anti-proliferative cytotoxic effect of cholecalciferol-loaded CCFB against the tumor cells may be due to its role in enhancing the cellular resilience and reducing oxidative stress. These results support the biocompatibility of the cholecalciferol-loaded CCFB system, making it a promising candidate for bone-targeted therapeutic applications.

Based on the data in Table 2, Trypan blue staining revealed that MG-63 cells treated with both CCFB and cholecalciferol-loaded CCFB exhibited a concentration-dependent increase in the percentage of non-viable cells, reflecting reduced cell proliferation at higher doses. At lower concentrations (10 and 25 μg mL^{-1}), both materials showed minimal cytotoxicity, with

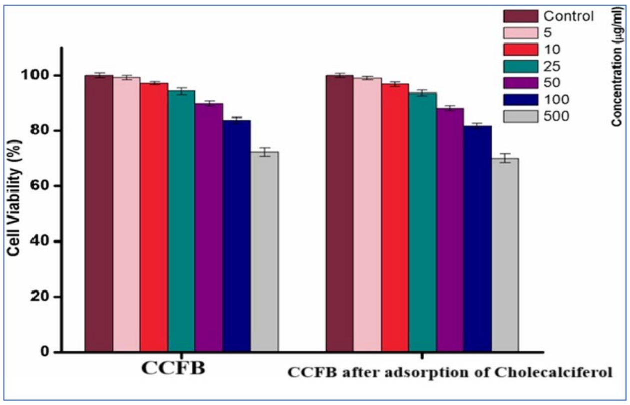

Fig. 11 Cell viability (%) of MG-63 cells treated with CCFB and cholecalciferol-loaded CCFB at various concentrations (5–500 μg mL^{-1}) after 24 h incubation. Data presented as mean ± SD ($n = 3$).

Table 2 Percentage of yrypan-blue reactive "non-viable" cells in MG-63 cells after treatment with CCFB or CCFB-loaded cholecalciferol for 24 h

	10 μg mL^{-1}	25 μg mL^{-1}	50 μg mL^{-1}	100 μg mL^{-1}	500 μg mL^{-1}
CCFB	0	0	20	35	40
CCFB loaded cholecalciferol	0	10	25	42	50
Reduction in cell growth	Negative	Negative	Negative	Mild	Moderate

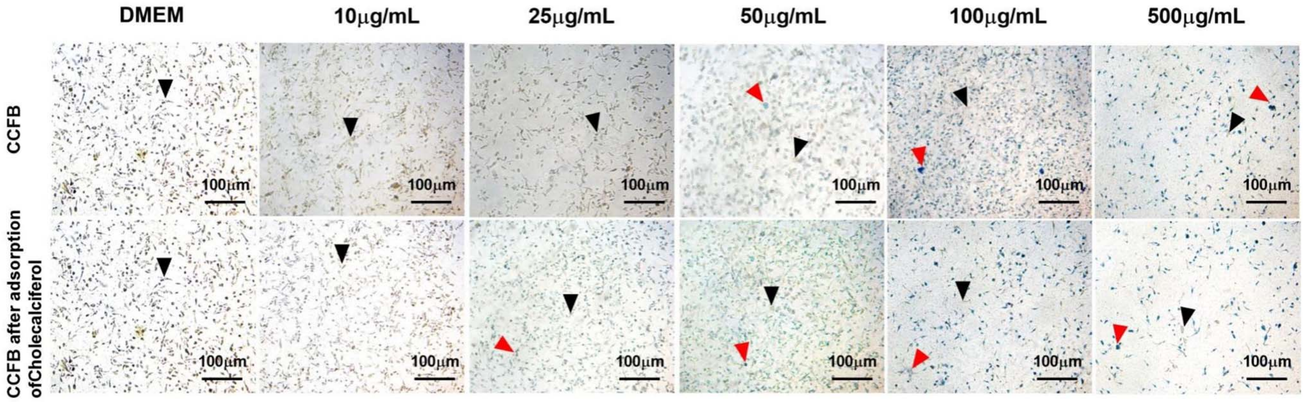

Fig. 12 MG-63 cells treated with CCFB and cholecalciferol-loaded CCFB for 24 h, assessed by trypan blue exclusion assay. Black arrowhead pointed a viable cell (trypan blue negative), while red arrowhead points to Trypan-blue positive (blue cells), which presents non-viable cells.

0% non-viable cells for CCFB and only 10% at 25 μg mL^{-1} for the cholecalciferol-loaded formulation indicating excellent biocompatibility and no reduction in cell growth. However, at 50 μg mL^{-1} and above, a progressive increase in cell death was observed. Notably, at 100 μg mL^{-1} and 500 μg mL^{-1}, cholecalciferol loaded CCFB resulted in higher percentages of non-viable cells (42% and 50%, respectively) compared to CCFB alone (35% and 40%), suggesting that the addition of cholecalciferol may slightly enhance cytotoxic effects at elevated concentrations. Overall, these results demonstrate a mild to moderate reduction in cell growth at higher concentrations, with both materials showing good biocompatibility at ≤25 μg mL^{-1} Fig. 12.

3.3 Antimicrobial study of CCFB before and after loading of cholecalciferol

Initial screening of growth conditions revealed that *S. aureus* exhibited robust proliferation in TSB broth, reaching an absorbance of approximately 1.8 at 600 nm after 200 minutes, compared to 1.2 in DMEM media. This difference indicates TSB provides a more nutrient-rich environment for bacterial growth. The correlation between optical density and colony-forming units (CFUs) was established, with CFU counts reaching 1.0×10^8 CFU mL^{-1} at OD 0.8 for cholecalciferol-enhanced cultures, compared to 1.5×10^8 CFU mL^{-1} for CCFB alone (Fig. 13a and b). The antimicrobial evaluation of CCFB and CCFB-cholecalciferol against *S. aureus* in DMEM: F12 cell culture media demonstrated concentration-dependent bacterial inhibition with marked differences between treatments (Fig. 13 c and d). Importantly, CCFB alone exhibited inherent antimicrobial activity, achieving moderate bacterial reduction across all tested concentrations, indicating the calcium carbonate matrix contributes to bacterial inhibition through cell wall disruption mechanisms. However, CCFB-cholecalciferol exhibited significantly superior antibacterial activity, with the 5 μg mL^{-1} concentration demonstrating the most substantial inhibitory effect and sustained CFU reduction throughout the incubation period. The enhanced performance of the cholecalciferol-loaded system compared to CCFB alone confirms a genuine synergistic effect rather than simple additive antimicrobial properties, suggesting complementary mechanisms of action between the mineral carrier and the bioactive compound. Statistical analysis using Student's *t*-test revealed significantly greater *S. aureus* viability reduction for CCFB-cholecalciferol at concentrations ≥2 μg mL^{-1} ($p < 0.05$) as detailed in Table S4. The most pronounced differences occurred at higher concentrations: at 4 μg mL^{-1}, mean log CFU mL^{-1} values were 4.30 ± 0.10 for CCFB *versus* 3.10 ± 0.10 for CCFB-cholecalciferol ($p = 0.004$), while at 5 μg mL^{-1}, CCFB-cholecalciferol reduced bacterial counts to 1.30 ± 0.09 log CFU mL^{-1} compared to 3.00 ± 0.11 log CFU mL^{-1} for CCFB alone ($p = 0.001$). This >10-fold enhancement in bacterial reduction at the highest concentration definitively establishes that the antimicrobial activity results from synergistic interactions between CCFB and cholecalciferol, rather than individual component effects. The 4-log reduction in *S. aureus* viability achieved by CCFB-cholecalciferol at 5 μg mL^{-1} (Fig. 13d) significantly outperforms CCFB alone (1.5-log reduction), confirming true synergy beyond additive effects. This enhanced efficacy stems from complementary mechanisms: CCFB's pore-driven physical disruption of bacterial membranes[56] combined with cholecalciferol's immunomodulation of antimicrobial peptides.[54,55] Crucially, this mineral-vitamin D_3 synergy differs fundamentally from chitosan-based systems that show only 85% inhibition despite relying solely on electrostatic binding. The enhanced antimicrobial activity of cholecalciferol-loaded CCFB is consistent with established literature demonstrating vitamin D_3's direct and indirect antimicrobial effects through immune response modulation and bacterial membrane disruption.[72,73] The observed synergy likely results from the combined action of the mineral matrix disrupting bacterial cell walls,[74] and cholecalciferol's immunomodulatory properties enhancing infection control.[75] While vancomycin demonstrated potent antimicrobial activity as expected (achieving complete bacterial inhibition at 2 μg mL^{-1}), cholecalciferol-loaded CCFB showed promising efficacy that approached clinically relevant levels, particularly at higher concentrations. This suggests potential applications in combination therapies or as an alternative in cases where antibiotic resistance is a concern. These findings align with previous studies utilizing calcium-based biomaterials for antimicrobial applications,[76] and support the potential of marine waste-derived materials as cost-effective, sustainable antimicrobial agents.[77] The CCFB carrier system not only improves cholecalciferol stability and enables controlled release but also leverages the inherent biocompatibility and bioactivity of marine-derived calcium carbonate.[78] This dual functionality positions CCFB-cholecalciferol composites as promising candidates for biomedical applications requiring both antimicrobial and osteogenic properties, particularly in bone infection management and wound healing. Staphylococcus aureus was selected as the model organism for antimicrobial testing in this study due to its well-established clinical significance as a leading cause of biomaterial-associated and wound infections.[79–81] As a Gram-positive pathogen frequently implicated in post-surgical and device-related complications, *S. aureus* is widely recognized as a benchmark organism for initial evaluation of antimicrobial efficacy in novel biomaterial systems.[82–84] This approach is consistent with established protocols in the field, where *S. aureus* serves as a primary indicator of antibacterial performance, particularly

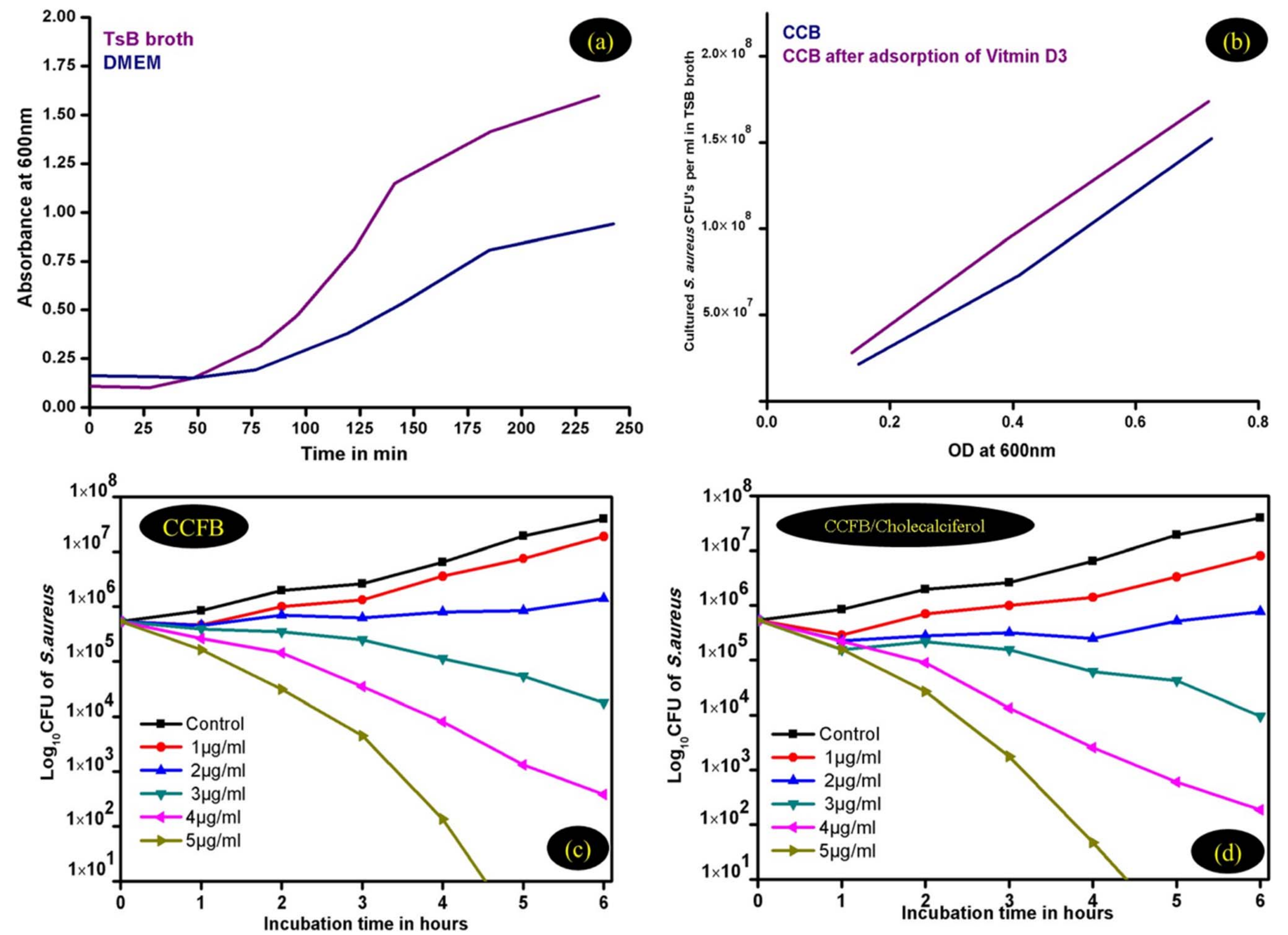

Fig. 13 (a) *S. aureus* growth curves in TSB broth and DMEM media. (b) Correlation of OD600 with CFU mL^{-1}. (c) Inhibition of *S. aureus* by CCFB at various concentrations. (d) Inhibition of *S. aureus* by CCFB after cholecalciferol loading at various concentrations. Data represent mean ± SD ($n = 3$). Statistical significance between CCFB and CCFB-Cholecalciferol at each concentration and time point was assessed by Student's *t*-test; $^{*}p < 0.05$, $^{**}p < 0.01$.

Table 3 Zone of inhibition diameters (mm) for CCFB and CCFB-cholecalciferol against *S. aureus* and MRSA[a]

Concentration (μg mL^{-1})	CCFB (mm)		CCFB-cholecalciferol (mm)		Vancomycin (mm)		
	S. aureus	MRSA	*S. aureus*	MRSA	*S. aureus*	MRSA	Negative control (mm)
1	7.9 ± 0.6	N/A	12.1 ± 1.0	N/A	10.1 ± 1.0	N/A	N/A
2	10.2 ± 0.3	N/A	15.6 ± 0.6	10.6 ± 0.4	13 ± 0.2	9.8 ± 0.4	N/A
3	12 ± 0.4	8.2 ± 0.9	19 ± 0.1	13.2 ± 0.7	16.2 ± 0.3	11.3 ± 0.1	N/A
4	13.8 ± 0.5	9.8 ± 0.2	22.8 ± 0.5	16.8 ± 0.8	19.3 ± 0.6	15.6 ± 0.9	N/A
5	16.4 ± 0.7	12.6 ± 0.6	25.7 ± 0.4	19.5 ± 0.1	21 ± 0.5	17.9 ± 0.3	N/A

[a] N/A: not applicable. Values are presented as mean ± standard deviation (SD) from triplicate experiments.

for materials intended for orthopedic, dental, and wound healing applications. While the present work focused on *S. aureus* to demonstrate proof-of-concept antimicrobial activity, it is recognized that comprehensive assessment of the antimicrobial spectrum requires evaluation against additional clinically relevant pathogens, including Gram-negative and multidrug-resistant strains. Future studies will therefore expand the antimicrobial testing panel to include organisms such as Escherichia coli and Pseudomonas aeruginosa, as well as resistant variants, to further elucidate the broad-spectrum efficacy and potential clinical applications of cholecalciferol-loaded CCFB.

3.3.1 Kirby–Bauer disk diffusion assay. To provide a robust benchmark for antimicrobial potency, vancomycin which is a clinically established antibiotic for *S. aureus* that was included as a positive control at concentrations matching the test materials (1–5 μg mL^{-1}). Following the incubation period, the antimicrobial activity of CCFB and CCFB-cholecalciferol was assessed by measuring the diameter of the zones of inhibition around each disk. The results are summarized in Table 3. The negative control disks (impregnated with sterile solvent) exhibited no zone of inhibition (data not shown), indicating no antimicrobial activity from the solvent itself. Conversely, the positive control disks containing vancomycin produced clear, well-defined zones of inhibition, confirming the susceptibility of *S. aureus* to this known effective antibiotic and validating the assay conditions.

As shown in Table 3, both CCFB and CCFB-cholecalciferol demonstrated concentration-dependent antimicrobial activity against *S. aureus* and MRSA stains, with increasing concentrations leading to larger zones of inhibition. CCFB alone exhibited measurable zones of inhibition, ranging from 7.9 ± 0.6 mm at 1 μg mL^{-1} to 16.4 ± 0.7 mm at 5 μg mL^{-1}. Similarly, MRSA was resistant to CCFB at concentrations more than 2 μg mL^{-1} (3–5 μg mL^{-1}) and exhibited zones of inhibition that ranged from 8.2 ± 0.9 for concentration of 3 μg mL^{-1} and 12.6 ± 0.6 for concentration of 5 μg mL^{-1}. On the other hand, concentrations lower than 3 μg mL^{-1} were resistant to the action of CCFB when compared to the reference antibiotic (vancomycin at 5 μg mL^{-1}) which showed activity against the tested pathogens where the zone of inhibition recorded as 21 ± 0.5 and 17.9 ± 0.3 for *S. aureus* and MRSA respectively. Regarding to the present results, Allogmani *et al.* 2023 observed that the tested nanocomposite material presented an excellent antibacterial activity against *S. aureus* strain.[85] Crucially, CCFB-cholecalciferol consistently exhibited significantly larger zones of inhibition compared to CCFB alone across all tested concentrations. At 1 μg mL^{-1}, CCFB-cholecalciferol showed a zone of 12.1 ± 1.0 mm, which increased to 25.7 ± 0.4 mm at 5 μg mL^{-1}. This enhanced activity is visually evident as more expansive clear areas around the disks containing the cholecalciferol-loaded compound. For instance, at 5 μg mL^{-1}, the zone of inhibition for CCFB-cholecalciferol (25.7 ± 0.4 mm) was substantially larger than that for CCFB alone (16.4 ± 0.7 mm), demonstrating a marked improvement in antimicrobial efficacy. Vancomycin, used as a positive control, also showed concentration-dependent activity, with zones ranging from 10.1 ± 1.0 mm at 1 μg mL^{-1} to 21 ± 0.5 mm at 5 μg mL^{-1}. Notably, at higher concentrations (*e.g.*, 4 and 5 μg mL^{-1}), the antimicrobial activity of CCFB-cholecalciferol (22.8 ± 0.5 mm and 25.7 ± 0.4 mm, respectively) surpassed or was comparable to that of vancomycin (19.3 ± 0.6 mm and 21 ± 0.5 mm, respectively at the same concentrations, highlighting its potent antibacterial effect as shown in Fig. 14. Moreover, MRSA strain was resistant to CCFB-cholecalciferol at 1 μg mL^{-1} but at higher concentrations the CCFB-cholecalciferol showed a remarkable antibacterial activity when compared to the reference antibiotic (vancomycin 5 μg mL^{-1}). From the results in Fig. 14, it was obvious that by increasing the concentration of CCFB-cholecalciferol (from 2 to 5 μg mL^{-1}). The antimicrobial activity was increased. The present study is in agreement with the similar findings of Diab *et al.* 2022 who evaluated the effect of hyaluronic acid/carboxymethyl chitosan embedded gold nanoparticles on Gram positive bacterial strains.[86] Orabi *et al.* 2022 also found that a mixture compound of silver nanoparticles with sesame oil showed a good antibacterial activity against *Staphylococcus aureus*.[87] Statistical analysis confirmed that the addition of cholecalciferol to CCFB resulted in a significant enhancement of antimicrobial efficacy at all tested concentrations, while the negative control showed no inhibition, validating the specificity of the assay.

The results from the Kirby–Bauer disk diffusion assay provide compelling visual and quantitative evidence of the antimicrobial efficacy of both CCFB and, more significantly, the enhanced activity achieved by loading cholecalciferol onto the CCFB carrier. The consistent observation of concentration-

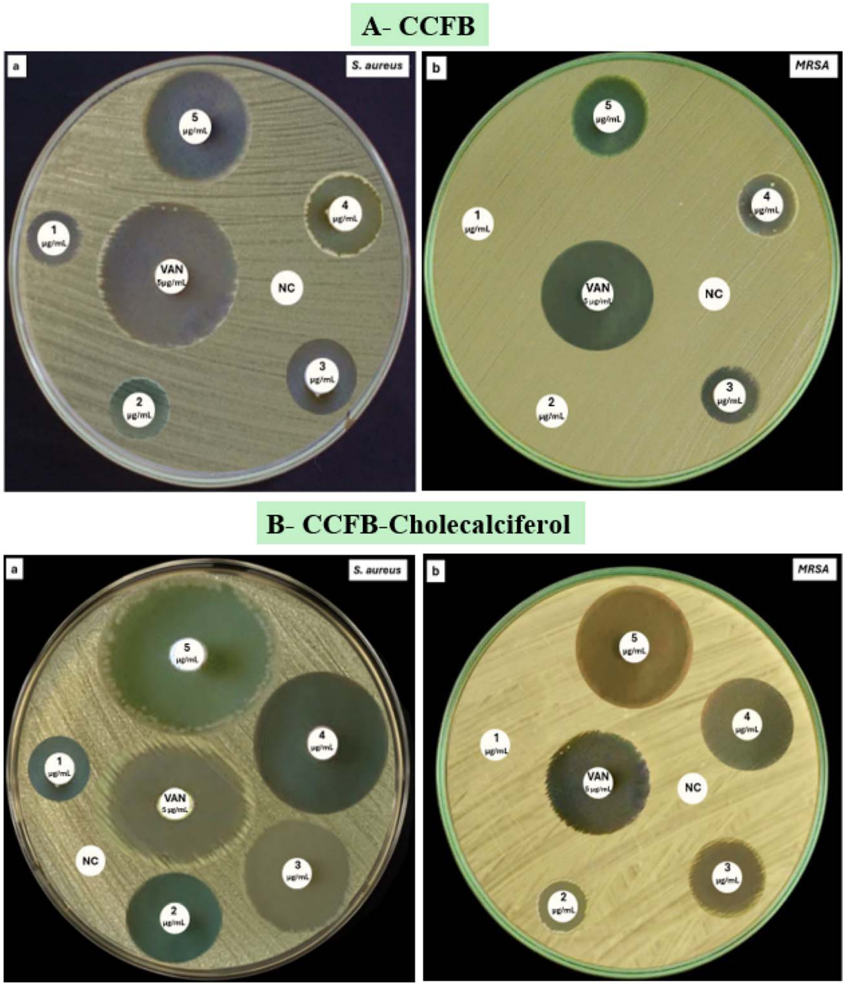

Fig. 14 Paper disc diffusion method showing zone of inhibition of the tested compounds (CCFB) against *S. aureus* and MRSA (Aa and Ab respectively) and CCFB loaded with cholecalciferol (CCFB- cholecalciferol) against *S. aureus* and MRSA (Ba and Bb respectively) at concentrations of 1, 2, 3, 4, and 5 µg mL^{-1} alongside negative control disks (sterile solvent) and positive control discs (vancomycin [VAN], 5 µg mL^{-1}).

dependent zones of inhibition for both compounds confirms their inherent antibacterial properties against *S. aureus*. The measurable zones of inhibition for CCFB alone support the premise that the calcium carbonate matrix possesses intrinsic antimicrobial capabilities, likely stemming from mechanisms such as physical disruption of bacterial cell walls or interference with membrane integrity.[88] This inherent activity forms a foundational component of the overall antimicrobial effect. However, the most striking finding is the consistently larger and more pronounced zones of inhibition exhibited by CCFB-cholecalciferol across all tested concentrations. This substantial enhancement, particularly evident at higher concentrations where the zone diameters significantly surpassed those of CCFB alone, strongly indicates a synergistic interaction between the CCFB carrier and cholecalciferol. This synergy is likely multifaceted. Cholecalciferl is well-documented for its direct antimicrobial effects, including its ability to disrupt bacterial membranes, and its indirect role in modulating host immune responses to enhance pathogen clearance.[72] The combination of the mineral matrix's disruptive action and cholecalciferol's direct and immunomodulatory properties create a potent dual-action antimicrobial system. Furthermore, the sustained release profile of cholecalciferol from the CCFB carrier, as suggested by the original study, could contribute to the sustained and superior inhibitory effect observed in these disk diffusion assays, translating into larger and more stable zones of inhibition.[89] Comparing the activity of CCFB-cholecalciferol to the vancomycin positive control provides a critical benchmark. While vancomycin, a well-established and potent antibiotic, demonstrated robust activity, the ability of CCFB-cholecalciferol to achieve comparable or even superior zone diameters at higher concentrations (*e.g.*, 4 and 5 µg mL^{-1}) is highly significant. This suggests that the cholecalciferol-loaded CCFB composite possesses a potent antibacterial effect that approaches clinically relevant levels. This finding is particularly promising given the increasing concerns regarding antibiotic resistance, positioning CCFB-cholecalciferol as a potential alternative or complementary agent in antimicrobial strategies.[89] These results are consistent with previous research on calcium-based biomaterials for antimicrobial applications and

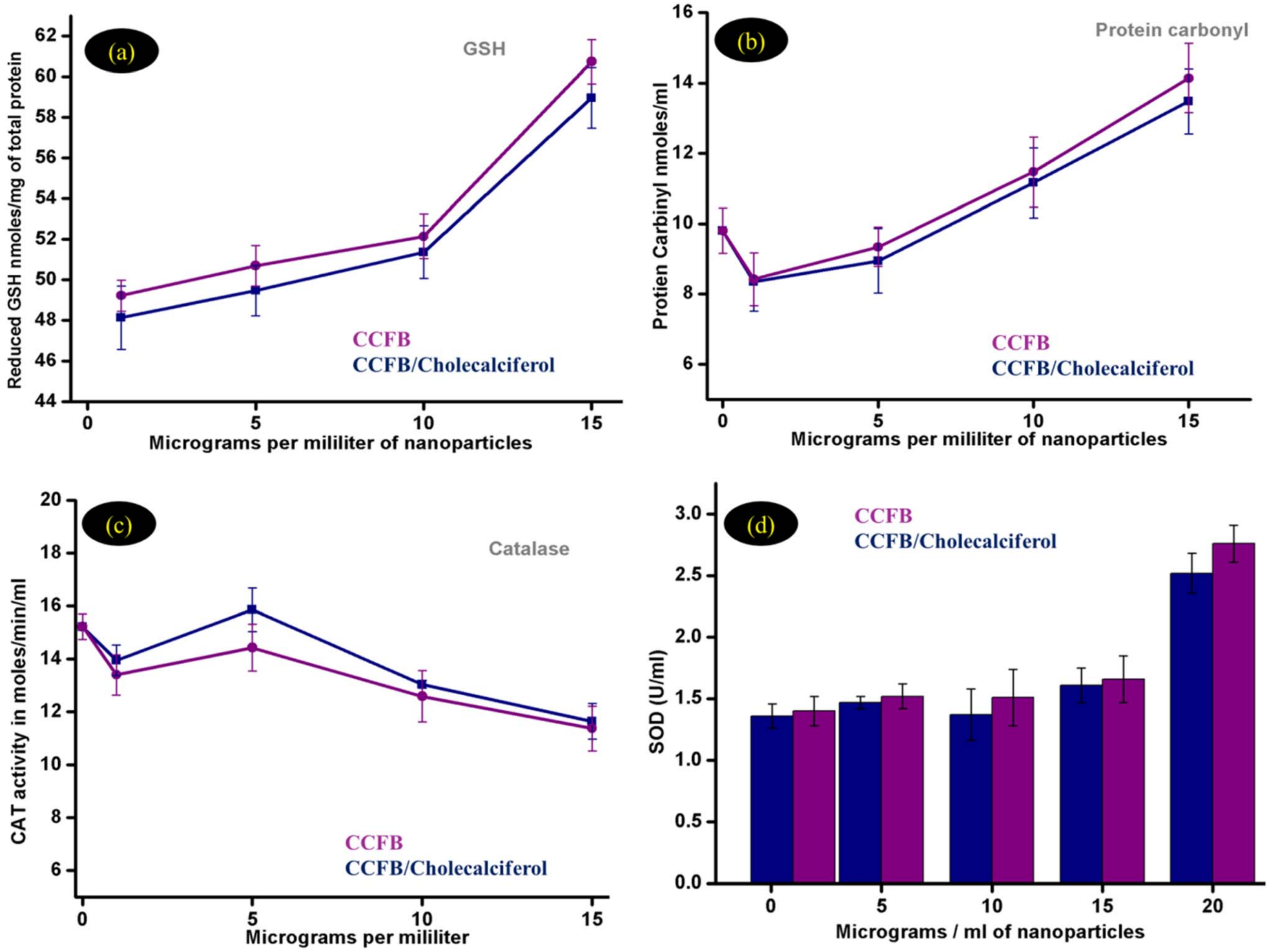

Fig. 15 CCFB and CCFB after loading of Cholecalciferol toxicity experiments were performed to measure toxicity (a) reduced glutathione GSH, (b) protein carbonyl content, and (c) catalase activity. (d) Superoxide dismutase activity (SOD): osteoblast cell extract was measured for SOD activity. Each experiment was done in triplicate; each bar represents the mean value ± S.E.M.

further support the utility of marine waste-derived materials as sustainable and cost-effective antimicrobial agents.[90–93] While the enhanced antimicrobial activity of cholecalciferol-loaded CCFB could involve membrane disruption or metabolic inhibition, we acknowledge these mechanisms require further validation. However, the observed synergy is distinct from chitosan-based systems in both material composition and mode of action. Unlike chitosan carriers that rely on cationic electrostatic binding,[94,95] CCFB functions as a mineral matrix (CaO/MgO) that physically compromises bacterial membranes through pore-mediated disruption.[96,97] This mineral action combines with cholecalciferol's immunomodulatory effects[98–100] rather than operating through chitosan-like pathways. The novelty lies in transforming seafood waste into a synergistic platform where The mesoporous mineral scaffold enables sustained release (93% over 12 h *vs.* 80% in 3 h for chitosan systems[101]), waste valorization achieves 60% cost reduction *vs.* synthetic carrier[102–104] and dual functionality (antimicrobial + antioxidant) emerges from mineral-vitamin D_3 synergy, as shown in Table S5.

3.3.2 Oxidative stress.

Fig. 15 a illustrates that both CCFB and CCFB with Cholecalciferol show a dose-dependent increase in GSH levels. At baseline (0 μg mL^{-1}), the GSH levels for CCFB were around 47 nmoles mg^{-1}, while CCFB with Cholecalciferol showed slightly higher levels at 49 nmoles mg^{-1}. As the concentration increased to 5 μg mL^{-1}, GSH levels rose to 49 nmoles mg^{-1} for CCFB and 50 nmoles/mg for CCFB with cholecalciferol. This trend continued at 10 μg mL^{-1}, where GSH levels reached 52 nmoles mg^{-1} for CCFB and 54 nmoles/mg after loading cholecalciferol. At the highest concentration tested (15 μg mL^{-1}), GSH levels peaked at 59 nmoles mg^{-1} for CCFB and 62 nmoles/mg for CCFB with cholecalciferol. To determine whether these differences were statistically significant, student's *t*-test at each concentration was performed. The results indicated that the increase in GSH levels was statistically significant at 10 and 15 μg mL^{-1} ($p < 0.05$), supporting the enhanced antioxidant capacity of the cholecalciferol-loaded CCFB (Table S6).

In both conditions, including CCFB alone and CCFB after cholecalciferol loading, the protein carbonyl levels were measured at varying concentrations of nanoparticles (0, 5, 10, and 15 μg mL^{-1}). Initially, both conditions started at a similar protein carbonyl level of 10 nmoles ml^{-1}. As the concentration of samples increased, the protein carbonyl levels decreased to around 8 nmoLes ml^{-1} at 5 μg mL^{-1} (Fig. 15b). Statistical analysis revealed no significant difference between CCFB and CCFB-Cholecalciferol at any concentration ($p > 0.05$), suggesting that Cholecalciferol loading does not markedly alter the protein carbonyl response.

As shown in (Fig. 15c), the activity of CAT in CCFB before and after the loading of cholecalciferol under oxidative stress conditions was also assessed. Initially, at 0 μg mL^{-1}, the CAT activity is slightly higher in untreated CCFB compared to the vitamin D_3-loaded sample. As the concentration increases to 5 μg mL^{-1}, CAT activity decreases slightly for both samples, with untreated CCFB maintaining a marginally higher level. At 10 μg mL^{-1}, CAT activity peaks for both samples, with untreated CCFB showing a more pronounced peak. However, after cholecalciferol loading, the peak is lower, indicating a potential inhibitory effect or altered enzyme kinetics. Beyond this point, at 15 μg mL^{-1}, CAT activity declines for both samples. Statistical comparison showed that the differences in CAT activity between the two groups were not significant at any tested concentration ($p > 0.05$).

Fig. 15d illustrates the SOD activity of CCFB before and after cholecalciferol loading, across concentrations from 0 to 20 μg mL^{-1}. At 0 μg mL^{-1}, both untreated and cholecalciferol-loaded CCFB show similar SOD activity around 1.5 μg ml^{-1}. As sample concentration increases, SOD activity rises for both, with a more pronounced increase in cholecalciferol-loaded samples. At 5 and 10 μg mL^{-1}, the activity is slightly higher for cholecalciferol-loaded CCFB, and at 15 μg mL^{-1}, the difference becomes more distinct. The peak occurs at 20 μg mL^{-1}, where SOD activity reaches approximately 3.0 μg mL^{-1} for cholecalciferol-loaded CCFB, surpassing untreated CCFB. Statistical analysis confirmed that SOD activity was significantly higher in the cholecalciferol-loaded group at 15 and 20 μg mL^{-1} ($p < 0.05$), indicating a synergistic effect on antioxidant enzyme activation at higher concentrations.

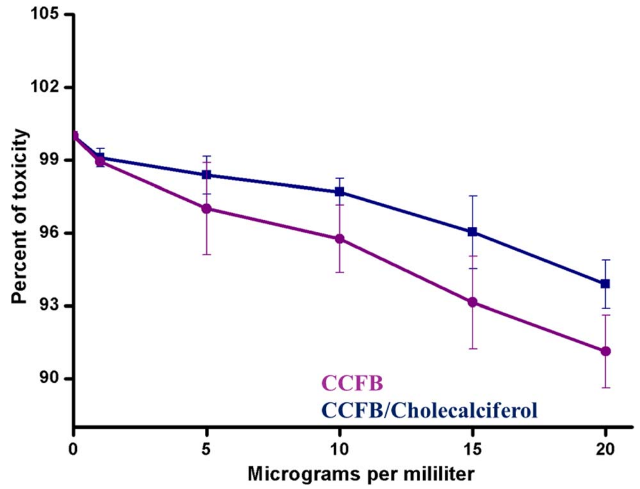

Fig. 16 LDH of CCFB and CCFB after loading of cholecalciferol. Each experiment was done in triplicate; each bar represents the mean value ± S.E.M.

3.3.3 LDH assay. Building on the demonstrated antimicrobial efficacy of cholecalciferol-loaded CCFB against S. aureus, next the biocompatibility and potential cytotoxic effects of these materials on mammalian cells using the LDH assay were evaluated. As shown in Fig. 16, the effect of cholecalciferol loading on the toxicity of CCFB was evaluated by measuring LDH activity. The results demonstrate a decrease in LDH activity (indicative of lower cytotoxicity) with increasing concentrations of both CCFB and cholecalciferol-loaded CCFB. Notably, CCFB loaded with cholecalciferol consistently exhibited significantly lower LDH release compared to CCFB alone across all tested concentrations (0–20 μg mL^{-1}). Statistical analysis indicated that this reduction was significant at concentrations ≥10 μg mL^{-1} ($p < 0.05$, Table S7).

These findings are in agreement with previous studies showing that cholecalciferol (vitamin D_3) can exert cytoprotective effects by reducing oxidative stress and stabilizing cellular membranes, thereby lowering LDH release.[72,73] Charoenngam and Holick demonstrated that vitamin D supplementation reduced LDH release and improved cell viability under oxidative conditions by upregulating antioxidant pathways and modulating inflammatory responses.[72] Similar trends have been reported for other calcium-based biomaterials, where the presence of bioactive ions supports cell survival and reduces cytotoxicity.[76,78] In particular, marine-derived calcium carbonate materials have shown good biocompatibility and low cytotoxicity, supporting their use as carriers in biomedical applications.[77] Compared to studies where certain nanomaterials increased LDH release due to membrane disruption or oxidative stress,[74] the recent results indicate that the CCFB-cholecalciferol composite not only avoids these adverse effects but also actively protects against cellular damage. The observed synergistic effect may be attributed to the combined benefits of the mineral matrix and the antioxidant, anti-inflammatory properties of vitamin D_3. This enhanced detoxifying property supports the potential application of CCFB-cholecalciferol as a safe and effective biomaterial for therapeutic use, particularly in bone tissue engineering and infection control. Overall, the findings align well with the literature, highlighting the novelty of using marine waste-derived CCFB in combination with cholecalciferol to achieve both antimicrobial and cytoprotective effects. Further studies are warranted to elucidate the underlying molecular mechanisms and to confirm these effects in in vivo models.

3.4 *In vitro* release study

The *in vitro* cumulative release profiles of free and CCFB-loaded cholecalciferol revealed distinctly different release behaviors, as illustrated in Fig. 17. Free cholecalciferol exhibited a rapid initial release, with 15.12% released within the first 5 minutes (0.083 h), increasing sharply to 42.12% by 30 minutes and plateauing at 98.46% by 36 hours. In contrast, the encapsulated form demonstrated a more sustained release, starting at 8.01%

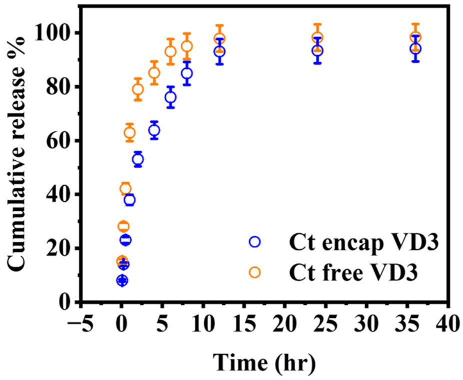

Fig. 17 Cumulative release of cholecalciferol (%) over time intervals for free cholecalciferol and cholecalciferol loaded on CCFB formulations in 0.1 N HCl.

at 5 minutes and reaching 23.04% at 30 minutes, with a gradual increase to 94.14% over 36 hours. At 12 hours, the release reached 93.06% for the encapsulated form compared to 97.92% for the free form. This controlled slower release is likely governed by the interaction of cholecalciferol with the porous structure of the CCFB matrix, which modulates diffusion and enables sustained delivery. Such a prolonged release profile is advantageous for enabling dual therapeutic and antimicrobial applications, as it can maintain effective vitamin D3 levels over extended periods while simultaneously supporting antimicrobial efficacy. This makes the CCFB-based formulation a promising multifunctional platform for advanced biomedical interventions where both systemic and local therapeutic actions are desired.

3.4.1 *In vitro* release kinetics. The *in vitro* release kinetics of cholecalciferol loaded onto calcinated cuttlefish bone (CCFB) were evaluated through various release models including zero-order kinetics, First-order kinetics, Korsmeyer–Peppas Model (power law), Higuchi model (diffusion-controlled release), revealing significant insights when compared to free cholecalciferol, as tabulated in Table 4. The zero-order and first-order models indicated that CCFB loading slower the initial release rate of cholecalciferol, as evidenced by lower K_o and K_1 values for CCFB-loaded cholecalciferol (1.051 and 0.002073, respectively) compared to the free form (0.824 and 0.006218, respectively). This suggests a slower release profile, potentially due to the interaction between cholecalciferol and the CCFB surface. The Korsmeyer–Peppas model, with a lower K value (0.302 *vs.* 0.473) and a n value closer to 0.5 for CCFB-loaded cholecalciferol (0.495 *vs.* 0.299), indicated that the release mechanism might involve both diffusion and erosion, whereas the free cholecalciferol likely follows a diffusion-dominant mechanism. In contrast, the Higuchi model showed a lower K_H value for CCFB-loaded cholecalciferol (10.843 *vs.* 12.263), pointing to a slower diffusion rate from the CCFB matrix compared to the free drug. Together, these findings suggest that CCFB loading not only slows the initial release of cholecalciferol but also alters its release kinetics, potentially due to the surface interaction between cholecalciferol and the porous CCFB, which might modify the diffusion and erosion processes, ultimately leading to a controlled release profile as shown in (Fig. 18).

3.5 Comparative analysis with calcium-based carriers

The comparative analysis (Tables S8 and S9) positions CCFB-Cholecalciferol as a uniquely sustainable and multifunctional alternative to conventional calcium-based carriers. Unlike synthetic hydroxyapatite (HAp) or β-TCP which require energy-intensive production and lack intrinsic bioactivity,[105,106] our waste-derived CCFB leverages seafood byproducts ($0.86 per g) to synergistically integrate antimicrobial, antioxidant, and cytoprotective functions. While HAp and β-TCP excel in bone regeneration but depend on dopants for antimicrobial effects,[107] and $CaCO_3$ suffers from rapid burst release,[108] CCFB-cholecalciferol's mesoporous structure (92.64 $m^2\ g^{-1}$) enables controlled cholecalciferol delivery (93% over 12 h *via* diffusion/erosion), enhancing its efficacy against *S. aureus* (4-log reduction) while reducing cytotoxicity (decreased by 50% LDH release). This multifunctionality coupled with superior biocompatibility (>75% cell viability at 500 μg mL^{-1})[109] and dual waste-valorization addresses key limitations of existing carriers, establishing CCFB-cholecalciferol as a cost-effective platform for therapeutic delivery, though broader pathogen testing.

3.6 Cost analysis

Since the cost-effective of the material used have major benefits for practical applications, estimating the cost of the manufactured materials is a crucial component of performance analysis. The cost estimate of CCFB for this investigation can be regarded as having no acquisition costs. Energy costs for the equipment, which included dryers, a ball mill, and a calcination furnace, were 2.88, 1.2, and 0.24 USD, respectively as shown in Table 5. The overall cost of CCFB is roughly 0.86 USD per g, with a yield of 5 g every batch. The cost analysis for this study showed that

Table 4 Kinetic parameters for free cholecalciferol and cholecalciferol loaded on CCFB

		Active ingredients	
Release kinetic model	Parameters	Cholecalciferol loaded on CCFB	Free cholecalciferol
Zero-order model	K_0	1.051	0.824
First-order model	K_1	0.002073	0.006218
Korsmeyer–peppas model	K	0.302	0.473
	n	0.495	0.299
Higuchi model	K_H	10.843	12.263

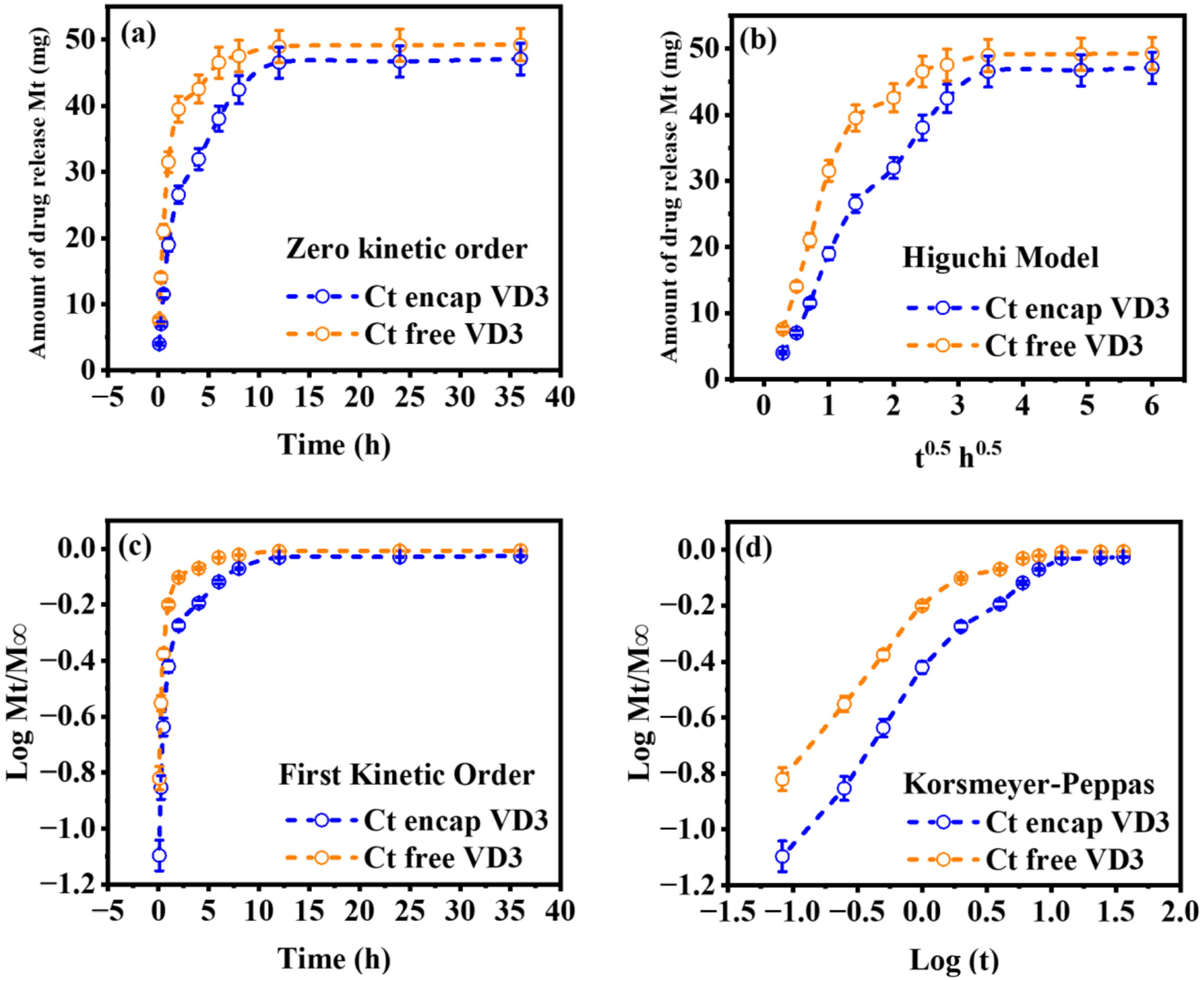

Fig. 18 Drug release data were fitted to various kinetic models: (a) zero-order, (b) first-order, (c) Korsmeyer–Peppas (Kors–Peppas), and (d) Higuchi, obtained from cholecalciferol adsorbed on CCFB and from free cholecalciferol.

Table 5 Cost and Energy Estimation of CCFB Preparation[a]

Equipment	Time (h)	Max. Power (kW)	Energy used (kWh)	Unit cost of power (USD per kWh)	Cost (USD)
Drying	12	1	12	0.24	2.88
Ball mill	5	1	5	0.24	1.20
Furnace	1	1	1	0.24	0.24
Total	—	—	18	—	4.32

[a] Yield per batch: 5 g. Total cost per gram: 0.86 USD per g. Total energy per gram: 3.6 kWh g. Total energy per kg: 3600 kWh kg.

CCFB was extremely cost-effective when compared to other water treatment adsorbents that have been reported previously, as shown in Table 6. In addition to being cost-effective, the preparation of CCFB in this study required a total of 18 kWh of energy per 5 g batch, corresponding to 3.6 kWh per gram or 3600 kWh per kilogram. This value is relatively high due to the small batch size and laboratory-scale conditions, which are typically less energy-efficient than industrial-scale processes. However, the use of seafood waste as a raw material eliminates acquisition costs and reduces the environmental burden by diverting waste from landfills. Compared to the production of synthetic hydroxyapatite, which generally requires more than twice as much energy, our process demonstrates both economic and environmental advantages. Future work will focus on process optimization and scaling up, which are expected to significantly reduce energy consumption per unit of product.

The energy consumption for CCFB preparation is 3.6 kWh g at laboratory scale, which is expected to decrease significantly at industrial scale due to improved efficiency and larger batch sizes.

Table 6 Evaluation of the prepared adsorbent's projected cost in relation to those published in the public domain

Material used	Cost (USD per g)	References
Zn–Fe LDH	3.12	110
Activated carbon	0.9	111
CaO/Zn Fe-LDH	5.47	112
LDH/PU/O-pom	0.927	113
Co/Ni/Cu–NH_2BDC MOF	7	114
Calcinated cuttle bone (CCFB)	0.86	This work

3.7 Study limitations

While this study highlights the promising potential of cholecalciferol-loaded CCFB as a multifunctional biomaterial, several limitations should be acknowledged. All biological evaluations, including antioxidant, antimicrobial, and cytocompatibility assessments, were performed *in vitro*; thus, the *in vivo* efficacy, pharmacokinetics, biodistribution, and long-term safety remain to be validated. The antimicrobial testing was restricted to *Staphylococcus aureus*, necessitating broader evaluations against Gram-negative bacteria, fungi, and biofilm-forming strains to fully characterize the therapeutic spectrum. Mechanistic insights into the antimicrobial action (such as bacterial membrane disruption or immunomodulatory pathways) were proposed but not experimentally confirmed; advanced characterization techniques including transmission electron microscopy (TEM) and metabolomics are recommended for future validation. Biocompatibility assessments relied on MTT assays, without qualitative analysis of cell adhesion or morphological response, which could be addressed using fluorescence or SEM imaging. Additionally, while preliminary cost estimations indicate the economic feasibility of CCFB, the scalability, life cycle impact, and regulatory compliance remain unassessed. These limitations outline clear directions for further optimization and validation.

3.8 Future prospects and translational potential of cholecalciferol-loaded CCFB biomaterial

This study establishes a proof-of-concept for repurposing seafood waste (specifically cuttlefish bone) into a cost-effective, sustainable, and multifunctional drug delivery platform. The cholecalciferol-loaded CCFB material demonstrated enhanced antioxidant, antimicrobial, and cytocompatibility properties, offering a viable alternative to synthetic polymers such as chitosan or PLGA, and expensive synthetic calcium phosphates. With a production cost estimated at $0.86 per gram and more than 60% cost savings compared to conventional carriers, the platform aligns with circular economy principles. Its porous, calcium-rich matrix supports high drug-loading and sustained release (94.14% over 36 hours), making it suitable for localized delivery in bone regeneration, wound healing, and infection prevention. Future research will involve expanding antimicrobial testing to Gram-negative and drug-resistant strains (*E. coli*, *P. aeruginosa*), as well as fungi. Mechanistic studies will explore cholecalciferol's immunomodulatory role and CCFB's structural effects using TEM and metabolomic profiling. Scaffold customization *via* polymer coatings or 3D printing will enable tailoring for different clinical indications starting from acute wound dressings to chronic bone infections. *In vivo* experiments in models of osteomyelitis and diabetic wounds will assess therapeutic efficacy, safety, and pharmacokinetics. To advance toward clinical translation, efforts will focus on optimizing manufacturing under GMP standards, performing comprehensive techno-economic and life cycle assessments, and engaging regulatory and industrial stakeholders. Ultimately, this approach offers a sustainable route to tackle major biomedical challenges such as antimicrobial resistance, bone loss, and healthcare costs, while simultaneously valorizing marine waste streams.

4 Conclusion

This study demonstrates that CCFB exhibits promising *in vitro* characteristics as a biocompatible antimicrobial and antioxidant agent, showing significantly enhanced inhibition of *Staphylococcus aureus* growth, improved antioxidant activity (increased GSH), reduced cytotoxicity (decreased LDH), and controlled release kinetics in cellular and bacterial models. These findings establish a proof-of-concept for transforming seafood waste into a multifunctional platform under controlled laboratory conditions, highlighting sustainable valorization potential. While these results suggest biomedical utility, clinical applications like bone regeneration require rigorous *in vivo* validation. Future work will prioritize animal studies, broad-spectrum pathogen testing, and mechanistic validation to advance this eco-friendly material toward therapeutic relevance. Additionally, the preliminary cost analysis underscores CCFB's potential as a low-cost, sustainable alternative to traditional polymeric carriers, which strengthens its promise for translation into scalable biomedical applications.

Conflicts of interest

All authors declare that they have no conflicts of interest to disclose.

Abbreviation

CFB	Cuttlefish bone
CCFB	Calcinated cuttlefish bone
SEM	Scanning electron microscopy
XRD	X-ray Diffraction
FTIR	Fourier transform infrared spectroscopy
BET	Brunauer–Emmett–Teller (surface area analysis)
TGA	Thermogravimetric analysis
DTG	Differential thermogravimetry
DMEM	Dulbecco's modified eagle medium
FBS	Fetal bovine serum
LDH	Lactate dehydrogenase
GSH	Glutathione

MTT	3-(4,5-dimethylthiazol-2-yl)-2,5-diphenyltetrazolium bromide
DMSO	Dimethyl sulfoxide
PBS	Phosphate buffered saline
NPs	Nanoparticles
S. aureus	*Staphylococcus aureus*
TSA	Tryptic soy agar
TSB	Tryptic soy broth
UV-Vis	Ultraviolet-visible (spectroscopy)
EDX	Energy dispersive X-ray spectroscopy
ATCC	American type culture collection
CFU	Colony forming unit
OD	Optical density
HCl	Hydrochloric acid
NaOH	Sodium hydroxide
$CaCO_3$	Calcium carbonate
Mg	Magnesium
Sr	Strontium
Cholecalciferol	Vitamin D_3

Data availability

The datasets generated and/or analyzed during this study are available from the corresponding author upon reasonable request.

Supplementary information is available. See DOI: https://doi.org/10.1039/d5ra04737d.

Acknowledgements

This work was supported and funded by the Deanship of Scientific Research at Imam Mohammad Ibn Saud Islamic University (IMSIU) (grant number IMSIU-DDRSP2501))

References

1 V. Venugopal and A. Sasidharan, Seafood industry effluents: Environmental hazards, treatment and resource recovery, *J. Environ. Chem. Eng.*, 2021, **9**, 104758, DOI: 10.1016/j.jece.2020.104758.
2 R. A. Al-Rawe, H. M. Al-Rammahi, A. Cahyanto, A. Ma'amor, Y. M. Liew, P. Sukumaran and W. N. W. Hassan, Cuttlefish-bone-derived biomaterials in regenerative medicine, dentistry, and tissue engineering: A systematic review, *J. Funct. Biomater.*, 2024, **15**, 219.
3 M. G. Rizzo, M. Briglia, V. Zammuto, D. Morganti, C. Faggio, F. Impellitteri, C. R. Multisanti and A. C. E. Graziano, Innovation in Osteogenesis Activation: Role of Marine-Derived Materials in Bone Regeneration, *Curr. Issues Mol. Biol.*, 2025, **47**, 175.
4 D. Yeoh, D. Johnston and D. C. Harris, *Squid and cuttlefish resources of Western Australia — Fisheries Research Report No. 314*, 2021, p. 101.
5 R. Gopal, M. Vijayakumaran, R. Venkatesan and S. Kathiroli, Marine organisms in Indian medicine and their future prospects, *Natural Product Radiance*, 2008, 139–145.
6 J. H. J. Diaz, R. D. Thilaga and V. Sivakumar, In-vitro cytotoxic activity of squid and cuttlefish bone extract on Hep G2 cell line, *Int. J. Pharm. Sci. Res.*, 2015, **6**, 778.
7 F. Cestari, F. Agostinacchio, A. Galotta, G. Chemello, A. Motta and V. M. Sglavo, Nano-hydroxyapatite derived from biogenic and bioinspired calcium carbonates: synthesis and in vitro bioactivity, *Nanomaterials*, 2021, **11**, 264.
8 J. Venkatesan, P. D. Rekha, S. Anil, I. Bhatnagar, P. N. Sudha, C. Dechsakulwatana, S.-K. Kim and M. S. Shim, Hydroxyapatite from cuttlefish bone: isolation, characterizations, and applications, *Biotechnol. Bioprocess Eng.*, 2018, **23**, 383–393.
9 S. M. Fathy, T. A. Elkhooly, A. A. Emam and F. M. Reicha, Evaluation of naturally derived hydroxyapatite tissue engineering scaffold coated with chitosan-carbon nanotubes composite, Egypt, *Dent. J.*, 2019, **65**, 463–474.
10 K. Pieklarz, M. Tylman and Z. Modrzejewska, Current progress in biomedical applications of chitosan-carbon nanotube nanocomposites: a review, *Mini Rev. Med. Chem.*, 2020, **20**, 1619–1632.
11 M. Fenice and S. Gorrasi, Advances in chitin and chitosan science, *Molecules*, 2021, **26**, 1805.
12 B. T. Iber, N. A. Kasan, D. Torsabo and J. W. Omuwa, A review of various sources of chitin and chitosan in nature, *J. Renew. Mater.*, 2022, **10**, 1097.
13 Q. Li, E. T. Dunn, E. W. Grandmaison and M. F. A. Goosen, Applications and properties of chitosan, in *Appl. Chitan Chitosan*, CRC Press, 2020: pp. 3–29.
14 S. Satitsri and C. Muanprasat, Chitin and chitosan derivatives as biomaterial resources for biological and biomedical applications, *Molecules*, 2020, **25**, 5961.
15 W. A. Pérez, J. A. Marín, J. N. López, M. A. Burgos and L. A. Rios, Development of a pilot-ecofriendly process for chitosan production from waste shrimp shells, *Environ. Process.*, 2022, **9**, 55.
16 A. K. Mallik, M. N. Sakib, M. Shaharuzzaman, P. Haque and M. M. Rahman, Chitin nanomaterials: preparation and surface modifications, in: *Handb. Chitin Chitosan*, Elsevier, 2020, pp. 165–194.
17 J. Chakravarty and T. A. Edwards, Innovation from waste with biomass-derived chitin and chitosan as green and sustainable polymer: a review, *Energy Nexus*, 2022, **8**, 100149.
18 S. Dasgupta, K. P. Reddy, P. Datta and A. Barui, Vitamin D3-incorporated chitosan/collagen/fibrinogen scaffolds promote angiogenesis and endothelial transition via HIF-1/IGF-1/VEGF pathways in dental pulp stem cells, *Int. J. Biol. Macromol.*, 2023, **253**, 127325.
19 A. A. Gupta, S. Kheur, R. V Badhe, A. T. Raj, R. Bhonde, A. Jaisinghani, N. Vyas, V. R. Patil, Y. A. Alhazmi and S. Parveen, Assessing the potential use of chitosan scaffolds for the sustained localized delivery of vitamin D, *Saudi J. Biol. Sci.*, 2021, **28**, 2210–2215.

20 E. A. Adekunle, O. O. Ayodele, A. O. Akala, E. M. Olorode, B. D. Agbejinmi, A. A. Ademola and R. I. Oyediran, A review of biofuel and biochemical production from forest and agricultural wastes, J. Res. For. Wildl, *Environ.*, 2020, **12**, 128–134.

21 I. Tlili, R. Bensghaier, L. Latrous El Atrache and A. Megriche, Cuttlefish bone powder as an efficient solid-phase extraction sorbent of anti-SARS-CoV-2 drugs in environmental water, *Chem. Pap.*, 2022, **76**, 6941–6951.

22 M. Fraga-Corral, P. Ronza, P. Garcia-Oliveira, A. G. Pereira, A. P. Losada, M. A. Prieto, M. I. Quiroga and J. Simal-Gandara, Aquaculture as a circular bio-economy model with Galicia as a study case: How to transform waste into revalorized by-products, *Trends Food Sci. Technol.*, 2022, **119**, 23–35.

23 N. V. Veríssimo, C. U. Mussagy, A. A. Oshiro, C. M. N. Mendonça, V. de Carvalho Santos-Ebinuma, A. Pessoa, R. P. de Souza Oliveira and J. F. B. Pereira, From green to blue economy: Marine biorefineries for a sustainable ocean-based economy, *Green Chem.*, 2021, **23**, 9377–9400.

24 S. M. Mahgoub, M. R. Shehata, F. L. Abo El-Ela, A. Farghali, A. Zaher and R. K. Mahmoud, Sustainable waste management and recycling of Zn–Al layered double hydroxide after adsorption of levofloxacin as a safe anti-inflammatory nanomaterial, *RSC Adv.*, 2020, **10**, 27633–27651, DOI: 10.1039/d0ra04898d.

25 S. M. Mahgoub, D. Essam, Z. E. Eldin, S. A. A. Moaty, M. R. Shehata, A. Farghali, S. E. B. Abdalla, S. I. Othman, A. A. Allam and F. I. A. El-Ela, Carbon supported ternary layered double hydroxide nanocomposite for Fluoxetine removal and subsequent utilization of spent adsorbent as antidepressant, *Sci. Rep.*, 2024, **14**, 3990.

26 S. M. Mahgoub, M. R. Shehata, A. Zaher, F. I. A. El-Ela, A. Farghali, R. M. Amin and R. Mahmoud, Cellulose-based activated carbon/layered double hydroxide for efficient removal of Clarithromycin residues and efficient role in the treatment of stomach ulcers and acidity problems, *Int. J. Biol. Macromol.*, 2022, **215**, 705–728.

27 S. Balu, M. V. Sundaradoss, S. Andra and J. Jeevanandam, Facile biogenic fabrication of hydroxyapatite nanorods using cuttlefish bone and their bactericidal and biocompatibility study, *Beilstein J. Nanotechnol.*, 2020, **11**, 285–295.

28 M. M. Mendes, K. Charlton, S. Thakur, H. Ribeiro and S. A. Lanham-New, Future perspectives in addressing the global issue of vitamin D deficiency, *Proc. Nutr. Soc.*, 2020, **79**, 246–251.

29 J. H. White, Emerging roles of vitamin D-induced antimicrobial peptides in antiviral innate immunity, *Nutrients*, 2022, **14**, 284.

30 A. F. Gombart, A. Pierre and S. Maggini, A review of micronutrients and the immune system–working in harmony to reduce the risk of infection, *Nutrients*, 2020, **12**, 236.

31 T. Ramezanli, B. E. Kilfoyle, Z. Zhang and B. B. Michniak-Kohn, Polymeric nanospheres for topical delivery of vitamin D3, *Int. J. Pharm.*, 2017, **516**, 196–203.

32 M. H. Asfour, S. H. Abd El-Alim, A. A. Kassem, A. Salama, A. S. Gouda, W. S. Nazim, N. H. Nashaat, M. Hemimi and N. Abdel Meguid, Vitamin D3-loaded nanoemulsions as a potential drug delivery system for autistic children: formulation development, safety, and pharmacokinetic studies, *AAPS PharmSciTech*, 2023, **24**, 58.

33 P. L. Colturato and D. Goveia, Controlled release of vitamin D3 using a nanocellulose-based membrane, *Sci. Rep.*, 2022, **12**, 12411.

34 R. P. Sharma, S. D. Shirsat, P. V Shinde, S. S. Mohite and R. S. Mane, Nano-antimicrobial Materials: Alternative Antimicrobial Approach, in: *Nanomater. Sustain. Dev. Oppor. Futur. Perspect.*, Springer, 2023, pp. 137–171.

35 A. M. Díez-Pascual, Recent progress in antimicrobial nanomaterials, *Nanomaterials*, 2020, **10**, 2315.

36 A. Sharma, N. Aggarwal, S. Rastogi, R. Choudhury and S. Tripathi, Effectiveness of platelet-rich fibrin in the management of pain and delayed wound healing associated with established alveolar osteitis (dry socket), *Eur. J. Dent.*, 2017, **11**, 508–513.

37 R. Hongsathavij, Y. Kuphasuk and K. Rattanasuwan, Clinical comparison of the stain removal efficacy of two air polishing powders, *Eur. J. Dent.*, 2017, **11**, 370–375.

38 W. Strober, Trypan blue exclusion test of cell viability, *Curr. Protoc. Immunol.*, 2015, **111**, A3–B.

39 Y. Wang, B. Ren, X. Zhou, S. Liu, Y. Zhou, B. Li, Y. Jiang, M. Li, M. Feng and L. Cheng, Growth and adherence of Staphylococcus aureus were enhanced through the PGE2 produced by the activated COX-2/PGE2 pathway of infected oral epithelial cells, *PLoS One*, 2017, **12**, e0177166.

40 M. Balouiri, M. Sadiki and S. K. Ibnsouda, Methods for in vitro evaluating antimicrobial activity: A review, *J. Pharm. Anal.*, 2016, **6**, 71–79.

41 C. A. Coleman, B. E. Hull, J. N. McDougal and J. V Rogers, The effect of m-xylene on cytotoxicity and cellular antioxidant status in rat dermal equivalents, *Toxicol. Lett.*, 2003, **142**, 133–142.

42 V. S. Babu, A. S. Reddy, P. M. Vasanth Kumar, C. Pallavi and C. Apparao, A Novel In-Vitro Dissolution Test For Cholecalciferol (D3) Tablets With Cumulative Drug Release Patterns At Altered Ph & Agitation, *Journal of Xi'an Shiyou University, Natural Science Edition*, 2022, **18**(8), 501–517.

43 P. Kumari and S. Dang, Development and in vitro characterization of diazepam loaded PLA nanoparticles, *Mater. Today Proc.*, 2020, **28**, 246–250.

44 J. Weng, H. H. Y. Tong and S. F. Chow, In vitro release study of the polymeric drug nanoparticles: development and validation of a novel method, *Pharmaceutics*, 2020, **12**, 732.

45 S. Modi and B. D. Anderson, Determination of drug release kinetics from nanoparticles: overcoming pitfalls of the dynamic dialysis method, *Mol. Pharm.*, 2013, **10**, 3076–3089.

46 N. B. E. Kumar, 1 M. Kumar, U. Kumar, A. K. Singh, U. Kumar and A. K. Singh, Therapeutic Nanoparticles: Recent Developments and Their Targeted Delivery Applications, *Nano Biomed. Eng.*, 2022, **14**, 38–52.

47 A. Thakuria, B. Kataria and D. Gupta, Nanoparticle-based methodologies for targeted drug delivery—an insight, *J. Nanoparticle Res.*, 2021, **23**, 87.

48 X. Zhang, A. Guo, X. Ma, H. Du, L. Yan, F. Hou and J. Liu, Cuttlefish-bone-structure-like lamellar porous fiber-based ceramics with enhanced mechanical performances, *ACS Appl. Mater. Interfaces*, 2023, **15**, 13121–13130.

49 A. C. Ferro and M. Guedes, Mechanochemical synthesis of hydroxyapatite using cuttlefish bone and chicken eggshell as calcium precursors, *Mater. Sci. Eng. C*, 2019, **97**, 124–140.

50 N. Suwannasingha, A. Kantavong, S. Tunkijjanukij, C. Aenglong, H.-B. Liu and W. Klaypradit, Effect of calcination temperature on structure and characteristics of calcium oxide powder derived from marine shell waste, *J. Saudi Chem. Soc.*, 2022, **26**, 101441.

51 K. U. Henggu, B. Ibrahim, P. Suptijah and J. Pengolah. Has, Hidroksiapatit dari cangkang sotong sebagai sediaan biomaterial perancah tulang, *Perikan. Indones.*, 2019, **22**, 1–13.

52 이용천 이상진, 윤영수, Characteristics of calcium phosphate powders synthesized from cuttlefish bone and phosphoric acid, *J. Ceram. Process. Res.*, 2007, 427–430.

53 F. Fayyazbakhsh, M. Solati-Hashjin, A. Keshtkar, M. A. Shokrgozar, M. M. Dehghan and B. Larijani, Release behavior and signaling effect of vitamin D3 in layered double hydroxides-hydroxyapatite/gelatin bone tissue engineering scaffold: An in vitro evaluation, *Colloids Surfaces B Biointerfaces*, 2017, **158**, 697–708, DOI: 10.1016/j.colsurfb.2017.07.004.

54 S. Khasim, Polyaniline-Graphene nanoplatelet composite films with improved conductivity for high performance X-band microwave shielding applications, *Results Phys*, 2019, **12**, 1073–1081, DOI: 10.1016/j.rinp.2018.12.087.

55 Ș. Țălu, K. Janus, S. Stach and A. S. Preparation, Nanoscale patterns in carbon – nickel nanocomposite thin films investigated by AFM and stereometric analysis, *Int. J. Mater.*, 2017, **4**, 54–62.

56 A. Elahi, W. Duncan, K.-C. Li, J. N. Waddell and D. Coates, Comparison of low and high temperature sintering for processing of bovine bone as block grafts for oral use: A biological and mechanical in vitro study, *Bioengineering*, 2023, **10**, 473.

57 E. Ferraz, J. A. F. Gamelas, J. Coroado, C. Monteiro and F. Rocha, Exploring the potential of cuttlebone waste to produce building lime, *Mater. Construcción*, 2020, **70**, e225.

58 S. Shang, K. L. Chiu, M. C. W. Yuen and S. Jiang, The potential of cuttlebone as reinforced filler of polyurethane, *Compos. Sci. Technol.*, 2014, **93**, 17–22, DOI: 10.1016/j.compscitech.2013.12.019.

59 A. Palaveniene, S. Tamburaci, C. Kimna, K. Glambaite, O. Baniukaitiene, F. Tihminlioğlu and J. Liesiene, Osteoconductive 3D porous composite scaffold from regenerated cellulose and cuttlebone-derived hydroxyapatite, *J. Biomater. Appl.*, 2019, **33**, 876–890, DOI: 10.1177/0885328218811040.

60 G. J. E. Poinern, R. Brundavanam, X. T. Le, S. Djordjevic, M. Prokic and D. Fawcett, Thermal and ultrasonic influence in the formation of nanometer scale hydroxyapatite bio-ceramic, *Int. J. Nanomedicine*, 2011, 2083–2095.

61 S. Liu, S. Sang, T. Wang, Y. Du, J. Jia and H. Fang, The effects of CO2 on organic groups in bituminous coal and high-rank coal via Fourier transform infrared spectroscopy, *Energy Explor. Exploit.*, 2018, **36**, 1566–1592.

62 O. G. Hussein, S. A. A. Moaty, W. A. Moselhy, A. A. Ahmed, K. Abdou and R. Mahmoud, Consecutive high-performance removal of Cu2+ metal ions and Deltamethrin using multifunctional pyrolysis cuttlebone/cotton fabric nanocomposite, *Int. J. Biol. Macromol.*, 2024, **270**, 132096.

63 E. Dadkhodazade, A. Mohammadi, S. Shojaee-Aliabadi, A. M. Mortazavian, L. Mirmoghtadaie and S. M. Hosseini, Yeast cell microcapsules as a novel carrier for cholecalciferol encapsulation: development, characterization and release properties, *Food Biophys*, 2018, **13**, 404–411.

64 K. Periasamy and G. C. Mohankumar, Sea coral-derived cuttlebone reinforced epoxy composites: Characterization and tensile properties evaluation with mathematical models, *J. Compos. Mater.*, 2016, **50**, 807–823.

65 N. Nouj, N. Hafid, N. El Alem, I. I. Buciscanu, S. S. Maier, P. Samoila, G. Soreanu, I. Cretescu and C. D. Stan, Valorization of β-chitin extraction byproduct from cuttlefish bone and its application in food wastewater treatment, *Materials (Basel)*, 2022, **15**, 2803.

66 K. Sankar and A. Achary, Bio-ceramic, mesoporous cuttlebone of Sepia officinalis is an ideal support for the immobilization of Bacillus subtilis AKL13 lipase: optimization, adsorption, thermodynamic and reaction kinetic studies, *Chem. Pap.*, 2020, **74**, 459–470.

67 E. Salama, F. I. A. El-Ela, W. H. Hassan, A. A. Farghali, A. A. Eweis, S. H. M. Hafez and R. Mahmoud, Eco-friendly innovation: Development of a multifunctional polyaniline-cuttlebone nanocomposite as a synergistic shield against doxorubicin-induced toxicity and a powerful antimicrobial agent, *Results Chem*, 2025, 102088.

68 F. Wang, W. Yu, C. Popescu, A. A. Ibrahim, D. Yu, R. Pearson, A. D. MacKerell and S. W. Hoag, Cholecalciferol complexation with hydroxypropyl-β-cyclodextrin (HPBCD) and its molecular dynamics simulation, *Pharm. Dev. Technol.*, 2022, **27**, 389–398.

69 M. Peydayesh, M. Bagnani, W. L. Soon and R. Mezzenga, Turning Food Protein Waste into Sustainable Technologies, *Chem. Rev.*, 2023, **123**, 2112–2154, DOI: 10.1021/acs.chemrev.2c00236.

70 B. Knechtle, Z. Jastrzębski, L. Hill and P. T. Nikolaidis, Vitamin D and Stress Fractures in Sport: Preventive and Therapeutic Measures-A Narrative Review, *Medicina (Kaunas)*, 2021, **57**(3), 223, DOI: 10.3390/medicina57030223.

71 A. V Mattioli, F. Coppi, P. Severino, C. Penna, P. Pagliaro, A. Dei Cas, V. Bucciarelli, R. Madonna, C. Tarperi, F. Schena, S. Cetrullo, T. Angelone, C. Rocca, A. Parenti, A. Palazzuoli, A. Margonato, S. Paolillo, P. Perrone Filardi, F. Barillà, C. Lombardi, M. Pinti, C. Molinari, A. Cevese, G. Novo, C. Pizzi, I. Porto, C. Poggesi, S. Gallina, G. Ambrosio and F. Fedele, A Personalized Approach to Vitamin D Supplementation in Cardiovascular Health Beyond the Bone: An Expert Consensus by the Italian National Institute for Cardiovascular Research, *Nutrients*, 2025, **17**(1), 115, DOI: 10.3390/nu17010115.

72 N. Charoenngam and M. F. Holick, Immunologic effects of vitamin D on human health and disease, *Nutrients*, 2020, **12**, 2097.

73 D. D. Bikle, Vitamin D metabolism, mechanism of action, and clinical applications, *Chem. Biol.*, 2014, **21**, 319–329.

74 M. Rinaudo, Chitin and chitosan: Properties and applications, *Prog. Polym. Sci.*, 2006, **31**, 603–632.

75 A. R. Martineau, D. A. Jolliffe, R. L. Hooper, L. Greenberg, J. F. Aloia, P. Bergman, G. Dubnov-Raz, S. Esposito, D. Ganmaa and A. A. Ginde, Vitamin D supplementation to prevent acute respiratory tract infections: systematic review and meta-analysis of individual participant data, *Bmj*, 2017, **356**.

76 H. D. Kim, S. Amirthalingam, S. L. Kim, S. S. Lee, J. Rangasamy and N. S. Hwang, Biomimetic materials and fabrication approaches for bone tissue engineering, *Adv. Healthc. Mater.*, 2017, **6**, 1700612.

77 S. Jana, P. Das, J. Mukherjee, D. Banerjee, P. R. Ghosh, P. K. Das, R. N. Bhattacharya and S. K. Nandi, Waste-derived biomaterials as building blocks in the biomedical field, *J. Mater. Chem. B*, 2022, **10**, 489–505.

78 Y. Zhang, M. Ni, M. Zhang and B. Ratner, Calcium phosphate—chitosan composite scaffolds for bone tissue engineering, *Tissue Eng.*, 2003, **9**, 337–345.

79 D. Campoccia, L. Montanaro and C. R. Arciola, The significance of infection related to orthopedic devices and issues of antibiotic resistance, *Biomaterials*, 2006, **27**, 2331–2339.

80 C. R. Arciola, D. Campoccia and L. Montanaro, Implant infections: adhesion, biofilm formation and immune evasion, *Nat. Rev. Microbiol.*, 2018, **16**, 397–409.

81 H. O. Gbejuade, A. M. Lovering and J. C. Webb, The role of microbial biofilms in prosthetic joint infections: A review, *Acta Orthop*, 2015, **86**, 147–158.

82 H. J. Busscher, Biomaterial-Associated Infection: Locating the Finish Line in the Race for the surface, *Sci. Transl. Med.*, 2012, **4**(153), 153rv10.

83 T. F. Moriarty, S. A. J. Zaat, H. J. Busscher, *Biomaterials Associated Infection: Immunological Aspects and Antimicrobial Strategies*, Springer Science & Business Media, 2012.

84 B. Li and T. J. Webster, Bacteria antibiotic resistance: New challenges and opportunities for implant-associated orthopedic infections, *J. Orthop. Res.*, 2018, **36**, 22–32.

85 A. S. Allogmani, R. M. Mohamed and M. S. Hasanin, Green, eco-friendly, highly biocompatible and bioactive nanocomposite-based biopolymers loaded with ZnO@ Fe3O4 nanoparticles, *Polymers (Basel)*, 2023, **15**, 3641.

86 S. F. Diab, M. M. Roushdy and M. Fouda, Hyaluronic acid/ carboxymethyl chitosan embedded gold nanoparticles modulate high fructose diet induced diabetes changes in rat, Egypt, *J. Chem.*, 2022, **65**, 183–193.

87 H. H. Elsayed, S. A. A. Orabi, S. E. Desouky, M. M. Roushdy, C. M. Sharaby and M. M. G. Fouda, In vitro and in vivo assessment of silver nanoparticles and sesame oil combination as in treatment of sodium nitrate-induced hepatotoxicity, *Egypt. J. Chem.*, 2022, **65**(10), 303–313.

88 G. Kasi and J. Seo, Influence of Mg doping on the structural, morphological, optical, thermal, and visible-light responsive antibacterial properties of ZnO nanoparticles synthesized via co-precipitation, *Mater. Sci. Eng. C*, 2019, **98**, 717–725.

89 K. M. Tyo, A. B. Lasnik, L. Zhang, M. Mahmoud, A. B. Jenson, J. L. Fuqua, K. E. Palmer and J. M. Steinbach-Rankins, Sustained-release Griffithsin nanoparticle-fiber composites against HIV-1 and HSV-2 infections, *J. Control. Release*, 2020, **321**, 84–99.

90 S. V Dorozhkin, Biocomposites and hybrid biomaterials based on calcium orthophosphates, *Biomatter*, 2011, **1**, 3–56, DOI: 10.4161/biom.1.1.16782.

91 S. S. Silva, E. M. Fernandes, L. C. Rodrigues, R. L. Reis, in *Antimicrobial Marine-Derived Materials BT - Handbook of the Extracellular Matrix: Biologically-Derived Materials*, F. R. Maia, J. M. Oliveira, R. L. Reis, Springer International Publishing, Cham, 2024, pp. 1173–1206. DOI: 10.1007/978-3-031-56363-8_56.

92 R. Kamphof, R. N. O. Lima, J. W. Schoones, J. J. Arts, R. G. H. H. Nelissen, G. Cama and B. G. C. W. Pijls, Antimicrobial activity of ion-substituted calcium phosphates: A systematic review, *Heliyon*, 2023, **9**, e16568, DOI: 10.1016/j.heliyon.2023.e16568.

93 D. Bharathi and J. Lee, Recent Advances in Marine-Derived Compounds as Potent Antibacterial and Antifungal Agents: A Comprehensive Review, *Mar. Drugs*, 2024, **22**(8), 348, DOI: 10.3390/md22080348.

94 H. Yilmaz Atay, Antibacterial Activity of Chitosan-Based Systems, *Funct. Chitosan Drug Deliv. Biomed. Appl.*, 2020, 457–489, DOI: 10.1007/978-981-15-0263-7_15.

95 C.-L. Ke, F.-S. Deng, C.-Y. Chuang and C.-H. Lin, Antimicrobial Actions and Applications of Chitosan, *Polymers (Basel)*, 2021, **13**(6), 904, DOI: 10.3390/polym13060904.

96 Y. He, S. Ingudam, S. Reed, A. Gehring, T. P. Strobaugh and P. Irwin, Study on the mechanism of antibacterial action of magnesium oxide nanoparticles against foodborne pathogens, *J. Nanobiotechnology*, 2016, **14**, 54, DOI: 10.1186/s12951-016-0202-0.

97 N.-Y. T. Nguyen, N. Grelling, C. L. Wetteland, R. Rosario and H. Liu, Antimicrobial Activities and Mechanisms of Magnesium Oxide Nanoparticles (nMgO) against Pathogenic Bacteria, Yeasts, and Biofilms, *Sci. Rep.*, 2018, **8**, 16260, DOI: 10.1038/s41598-018-34567-5.

98 A. Golpour, S. Bereswill and M. M. Heimesaat, Antimicrobial and immune-modulatory effects of vitamin D provide promising antibiotics-independent approaches to tackle bacterial infections–lessons learnt from a literature survey, *Eur. J. Microbiol. Immunol.*, 2019, **9**, 80–87.

99 N. Sanlier and M. Guney-Coskun, Vitamin D, the immune system, and its relationship with diseases, Egypt, *Pediatr. Assoc. Gaz.*, 2022, **70**, 39, DOI: 10.1186/s43054-022-00135-w.

100 R. F. Chun, P. T. Liu, R. L. Modlin, J. S. Adams and M. Hewison, Impact of vitamin D on immune function: lessons learned from genome-wide analysis, *Front. Physiol.*, 2014, **5**, 151.

101 R. Onnainty, B. Onida, P. Páez, M. Longhi, A. Barresi and G. Granero, Targeted chitosan-based bionanocomposites for controlled oral mucosal delivery of chlorhexidine, *Int. J. Pharm.*, 2016, **509**, 408–418, DOI: 10.1016/j.ijpharm.2016.06.011.

102 V. Venugopal, Valorization of seafood processing discards: Bioconversion and bio-refinery approaches, *Front. Sustain. Food Syst.*, 2021, **5**, 611835.

103 F. L. W. Xia, S. Supri, H. Djamaludin, R. Nurdiani, L. L. Seng, K. W. Yin and K. Rovina, Turning waste into value: Extraction and effective valorization strategies of seafood by-products, *Waste Manag. Bull.*, 2024, **2**, 84–100.

104 V. Venugopal, Green processing of seafood waste biomass towards blue economy, *Curr. Res. Environ. Sustain.*, 2022, **4**, 100164.

105 T. S. Sampath Kumar, K. Madhumathi, Y. Rubaiya and M. Doble, Dual mode antibacterial activity of ion substituted calcium phosphate nanocarriers for bone infections, *Front. Bioeng. Biotechnol.*, 2015, **3**, 59.

106 I. da Silva Brum, J. J. de Carvalho, J. L. da Silva Pires, M. A. A. de Carvalho, L. B. F. Dos Santos and C. N. Elias, Nanosized hydroxyapatite and β-tricalcium phosphate composite: Physico-chemical, cytotoxicity, morphological properties and in vivo trial, *Sci. Rep.*, 2019, **9**, 19602.

107 D. Maršík, O. Maťátková, A. Kolková and J. Masák, Exploring the antimicrobial potential of chitosan nanoparticles: synthesis, characterization and impact on Pseudomonas aeruginosa virulence factors, *Nanoscale Adv*, 2024, **6**, 3093–3105.

108 X. Liu, X. Li, R. Zhang, L. Wang and Q. Feng, A novel dual microsphere based on water-soluble thiolated chitosan/mesoporous calcium carbonate for controlled dual drug delivery, *Mater. Lett.*, 2021, **285**, 129142.

109 E. Simpson, H. Sarwar, I. Jack and D. Lowry, Evaluation of the potential of chitosan nanoparticles as a delivery vehicle for gentamicin for the treatment of osteomyelitis, *Antibiotics*, 2024, **13**, 208.

110 M. Kamel, G. Abd El-fatah, A. Zaher, A. A. Farghali, S. I. Othman, A. A. Allam, H. A. Rudayni, A. M. Salah, M. E. M. Hassouna and R. Mahmoud, Cost-effective layered double hydroxides/conductive polymer nanocomposites for electrochemical detection of wastewater pollutants, *Chinese J. Anal. Chem.*, 2024, **52**, 100368.

111 A. Syafiuddin, S. Salmiati, J. Jonbi and M. A. Fulazzaky, Application of the kinetic and isotherm models for better understanding of the behaviors of silver nanoparticles adsorption onto different adsorbents, *J. Environ. Manage.*, 2018, **218**, 59–70.

112 A. Elrafey, A. A. Farghali, W. Kamal, A. A. Allam, Z. E. Eldin, H. A. Rudayni, H. E. Alfassam, A. A. Anwar, S. Saeed and R. Mahmoud, Cost-effective eggshell-modified LDH composite for caffeine adsorption, cytotoxicity and antimicrobial activity: exploring the synergy and economic viability in search processes, *RSC Adv.*, 2024, **14**, 33281–33300.

113 R. Abdelazeem, W. Kamal, Z. E. Eldin, M. A. Roshdy, A. A. Allam, S. Saeed, D. A. Tawab, S. I. Othman, A. E. Allah and A. M. Radalla, Exploring the potential of waste biomass of olive as an additive for layered double hydroxide/polyurethane as an effective and safe agent for the adsorption of drug residues: a bioremediation approach, *Mater. Adv.*, 2024, **5**, 9092–9106.

114 R. Abdelazeem, H. A. Younes, Z. E. Eldin, A. A. Allam, H. A. Rudayni, S. I. Othman, A. A. Farghali, H. M. Mahmoud and R. Mahmoud, A selective, efficient, facile, and reusable natural clay/metal organic framework as a promising adsorbent for the removal of drug residue and heavy metal ions, *Colloids and Interfaces*, 2024, **8**, 50.